Revised and extended benchmark results for Rayleigh scattering of sunlight in spherical atmospheres

Sergey Korkin[a, 1] , Eun-Su Yang[b], Robert Spurr[c], Claudia Emde[d], Nickolay Krotkov[e],

Alexander Vasilkov[b], David Haffner[b], Jungbin Mok[f], and Alexei Lyapustin[e]

[a] Universities Space Research Association GESTAR, Columbia, MD, USA.

[b] Science Systems and Applications Inc., Lanham, MD, USA.

[c] RT Solutions Inc., Cambridge, MA, USA.

[d] Meteorological Institute, Ludwig-Maximilians-University, Germany.

[e] NASA Goddard Space Flight Center, Greenbelt, MD, USA

[f] University of Maryland ESSIC, College Park, MD, USA

Contents

---

[1] Corresponding author: sergey.v.korkin@nasa.gov

Abstract

While most of traditional Earth-atmosphere satellite remote sensing relies on radiative transfer in the plane parallel geometry, effects of sphericity are important at high sun and view zenith angles. Broad understanding of these effects is limited and, contrary to the plane-parallel case, finding accurate numerical results to test spherical RT codes is not easy. This paper aims to partially fill in this gap. Using the full-spherical RT code MYSTIC (Monte Carlo), and the plane-parallel RT code VLIDORT (discrete ordinates) corrected for atmospheric sphericity in the single and multiple scattering, we reproduced with better accuracy and extended the benchmark results by *Adams* & *Kattawar* [1978].

Introduction

Radiative Transfer (RT) codes are key components in the satellite remote sensing retrieval algorithms [e.g., *Lyapustin*, 2018; *Dubovik*, 2019; *Sinyuk*, 2020]. In general, an RT model is a suite of scientific software for the numerical simulation of light scattering in the Earth's atmosphere-surface environment. The testing of any RT code against reliable (accurate and reproducible) benchmarks is an essential step in software development and lifetime maintenance. Benchmark data must be reported numerically with sufficient accuracy. This paper deals with benchmark results for RT codes that simulate multiple scattering of monochromatic solar light over black surface in a spherical atmosphere of the Earth. We deal only with Rayleigh scattering in the absence of any trace gas absorption, and we ignore the effects of polarization and solar rays bending due to atmospheric refraction.

In many retrieval applications, RT modeling has been done using a plane-parallel model [*Lenoble*, 1985; *Stamnes*, 2017]; this is feasible because the Earth radius, ~6370km, is much larger than a typical height for low Earth orbit (LEO) satellite platforms, for example ~700km for the NASA A-Train constellation. The plane-parallel approximation is usually assumed to be valid for the solar (SZA) and/or view (VZA) zenith angles not exceeding 75° [*McCartney*, 1976: p.105, Sec. 2.5.4 "Equivalent Paths: Spherical Earth"; *Lenoble*, 1993: p.235, Sec.15.2.3.1 "Ground-based measurements"], although the level of accuracy is unclear from these references. However, modern Earth observation systems often go beyond these constraints, including the EPIC instrument on the Deep Space Climate Observatory (DSCOVR) platform located at the Sun-Earth Lagrange L-1 point at 1.5M km orbit, operational meteorological geostationary satellites (at ~36K km orbit) including GOES-R, HIMAWARI , KOMPSAT and others. The consideration of Earth sphericity is important even for the low Earth orbit observations, e.g., from MODIS and VIIRS near Polar regions where the SZA is high, for the limb observations, e.g. from SCIAMACHY and OMPS Limb Profiler, as well as for the ground-based atmospheric remote sensing during early morning and late evening hours [*Holben*, 1998; *Tzortziou*, 2008]. In these situations, the differences in optical paths and the solar-view geometries between spherical and plane-parallel atmospheres can no longer be ignored (**Fig.1**). To remain accurate in these cases, RT codes must account for the curvature of the Earth's atmosphere (hereafter, *sphericity,* - hence "spherical model" as opposed to "plane-parallel model").

In addition to changes in the optical path, the zenith angles take different values at the top (TOA) and bottom (BOA) of atmosphere (**Fig.2**). For the MODIS maximum scan angle of 55°, VZA$_{TOA}$=63° and VZA$_{BOA}$=65°, which follows from

$$\sin \theta^{BOA} = \left(1 + \frac{h}{R_E}\right) \sin \theta^{TOA}. \tag{1}$$

The right panel in **Fig.2** shows the VZA to the scan angle ratio at TOA and BOA according to Eq.(1). For a plane-parallel atmosphere, all VZAs would be 55° for the MODIS maximum scan angle.
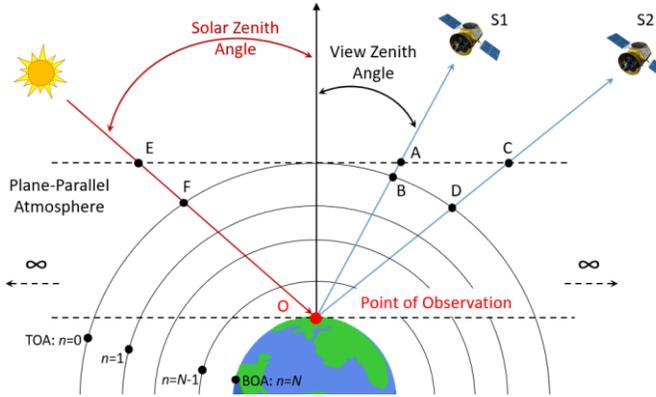
Fig.1: *The difference in the optical path between plane-parallel (dashed line) and spherical (solid line) atmospheres increases with larger VZA (segment AB for satellite position S1 and segment CD for position S2). The same effect applies to the solar beam (segment EF).*

In Eq.(1) and in the sequel, θ stands for the VZA, R_E = 6371 (km) is the mean Earth radius, and h (km) is an arbitrary height above the ground. Eq.(1) shows that $\theta_{BOA} \geq \theta_{TOA}$. At some critical angle VZA$_{TOA}$ given by

$$\theta_{TOA}^{Critical} = \sin^{-1}\left(\frac{R_E}{R_E + h}\right), \tag{2}$$

the line-of-sight (LOS) hits the ground at 90°. For any value of VZA$_{TOA}$ exceeding this critical angle, the line of sight goes horizontally through a tangent height in the atmosphere, something which is not possible in a plane-parallel medium. When the Earth is observed from a height h = 100km, the critical angle is $\theta_{Critical}^{TOA} \approx 79.9°$.
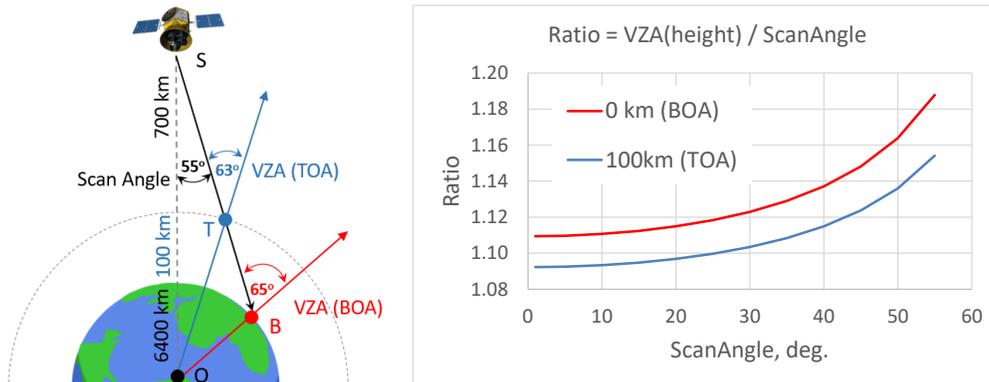
Fig.2: *In spherical geometry, the VZA for a point in atmosphere depends on the height (left image). For the NASA A-Train orbit at ~700km, a scan angle of 55° between the satellite nadir SO and the view direction SB corresponds to VZA=63° on TOA (point T) and VZA=65° on BOA (point B). The right panel shows the ratio of the VZA to the scan angle at TOA and BOA. For a plane-parallel atmosphere, all VZAs would be 55°.*

3

The exigencies of spherical geometry lead to the violation of several fundamental results in RT theory which are valid for plane-parallel media. For example, the principle of reciprocity

$$\mu\, I(\mu, \mu_0, \varphi) = \mu_0\, I(\mu_0, \mu, \varphi)\,, \tag{3}$$

where I is the intensity, μ, μ_0, and φ are the cosines of VZA, SZA, and azimuth, respectively, is no longer valid in a spherical medium. *Adams & Kattawar* [1978: p.151] note that for single scattering alone, the right hand side of Eq.(3) is up to 3 times higher than the left for Rayleigh scattering. Another example that is not valid for spherical media is the natural azimuth independence of the intensity for isotropically scattering plane-parallel atmospheres. In a spherical atmosphere, the scattered intensity always depends on the relative azimuth, except for the overhead sun configuration. The azimuthal asymmetry comes from the dependence of the direct solar beam attenuation factor on relative azimuth [*Herman*, 1995**a**: p.380].

The plane-parallel atmosphere is, by definition, horizontally infinite. It cannot deal with twilight, refraction, and the existence of the day/night line (terminator). These fundamental issues make it difficult to find a simple yet general sphericity correction factor, which can be applied to a plane-parallel RT model in order to generate radiation fields that are sufficiently close to spherical RT equivalents, in a wide range of applications. In this paper, we turn our attention to two RT codes that can simulate, precisely or approximately, multiple scattering of light in a spherical atmosphere. We leave aside detailed performance considerations (accuracy and runtime) of full-spherical and approximate plane-parallel RT codes, as well as the combing single and/or double scattering in spherical geometry with higher-order scattering from the plane-parallel RT model.

RT codes require validation against reliable numerical data published in the open literature. A complete literature review is almost impossible. However, our analysis of about 90 references published from the 1960's to the present day shows that there is a lack of accurate (numbers, not figures), reliable (easy to reproduce, with known accuracy), and general (different solar-view geometries and atmosphere-surface properties) benchmark results for spherical geometry. This paper aims to partially fill the gap by: 1) reproducing, with better accuracy, the existing benchmark results generated by *Adams* & *Kattawar* [1978: p.143, Table I], these being the most closely related to modern requirements for satellite remote sensing applications, and 2) extending their results beyond the principal plane using two state-of-the-art RT codes, a true-spherical Monte Carlo code MYSTIC from the libRadtran[2] package [*Mayer* & *Kylling*, 2005; *Mayer*, 2009; *Emde*, 2016] and the discrete ordinate VLIDORT code [*Spurr & Christi*, 2019] corrected for atmospheric sphericity. Both codes have been in existence for some time and are widely used in the remote sensing community. In this paper, we refer to the work by *Adams* & *Kattawar* [1978] as A&K.

The paper is structured as follows. First, in the "References overview", we highlight the need for publication of accurate benchmark results to test spherical RT codes. In the next section on "Methodology", we briefly describe the spherical RT implementation in MYSTIC (which is the baseline code in our research), and the discrete-ordinate treatment in VLIDORT. In the following section, we discuss the accuracy of the existing and new benchmarks ("Numerical results and discussion"). Aspects of spherical geometry as applied to RT are discussed in the Appendices. We conclude the paper with a Summary.

---

[2] www.libradtran.org (accessed June 12, 2020)

References Overview

Nowadays, the theory of light scattering in a spherical atmosphere has been well developed. Numerous papers contain mathematical formalisms, e.g. *Lenoble* [1961], *Bellman* [1969], *Smokty* [1969], to name just a few of the earliest. *Rozenberg* [1966: p.125, Chapter III "Principles of the twilight theory"] describes in detail the computation of optical paths in a spherical atmosphere but does not treat multiple scattering of light. The entire monograph by *Sen* & *Wilson* [1990] deals with RT in curved media, including Chapter VII "Numerical methods for transfer problems in spherical geometry" (p.321), which, despite that name, has no reported numerical results. *Sobolev* [1975: p.213, Chapter 11 "Spherical atmospheres"] calculates the brightness of a planet close to the terminator for the isotropic scattering case (p.229: Table 11.2), using an approximate numerical solution. His results agree qualitatively with observations of Venus, but the numerical accuracy is unclear. In Chapter 4 "Monte Carlo methods for solving direct and inverse problems of the theory of radiative transfer in a spherical atmosphere" of *Marchuk* [1980], there are extensive numerical results compared against measurements. In that work, realistic atmospheric models (gas absorption profiles, aerosol, surface reflectance, 14 wavelengths, etc.) were assumed. These "too realistic" scenarios are hard to reproduce with confidence. Also, the authors report ~10% simulation error (p.104), which is not acceptable for our goals in this paper. However, throughout the chapter, *Marchuk* and co-authors do present numbers for intensities as a function of the atmospheric and surface optical properties, location of the observer in the atmosphere, the role of polarization, and for single scattering. The work by *Kalkofen* [1984: p.235] contains a section on "Spherical radiative transfer" (Chapter II), but this book is hard to find and, as of now, we have not been able to check for the availability of numerical data. In Part II of *Lenoble* [1985: p.247], there is Chapter 3 "Spherical planetary atmospheres illuminated by the solar beam", again with no numerical results. The same can be said for Section 10.11 "Numerical Results" in *Natsuyama's* [1998] Chapter 10 "Transfer of Radiation with Spherical Symmetry" -this contains only figures. In the book by *Stamnes et al*. [2017: Appendix M[3]] there is a discussion on the influence of Earth curvature on the optical path and the Chapman function formalism [*Dahlback*, 1991]. The RT code DISORT [*Stamnes*, 1988] has used this technique for about three decades [*Mayer*, 1997; *He*, 2018], however we are not aware of published numerical data from the DISORT team [*Laszlo*, 2017].

Years of intensive theoretical studies coupled with the easy availability of computational resources have resulted in the development of several true- and pseudo-spherical RT codes. Most, if not all, plane-parallel techniques have been extended to the spherical case. This includes the Monte Carlo method [*Collins*, 1972; *Blättner*, 1974; *Adams*, 1978; *Ding*, 1994; *Oikarinen*, 1999; *Postylyakov*, 2004**ab**; *Davis*, 2005; *Spada*, 2006; *Emde*, 2007, -16; *Gratiy*, 2010**ab**; *Eriksson*, 2011; *Premuda*, 2012; *Buehler*, 2018; *Ramon*, 2019; *Zhuravleva*, 2019; *Ockenfuß*, 2019], discrete ordinates [*Dahlback*, 1991; *Belikov*, 2000; *Rozanov V*, 2002, 2014; *Spurr*, 2002, 2004, 2019; *Emde*, 2004; *Rozanov A*, 2005; *Doicu*, 2009**ab**] including low number of streams approximation [*Wilson*, 1980; *Kylling*, 1995; *van Oss*, 2002], two [*Natraj*, 2007] and successive orders of scattering [*McLinden*, 2002; *Bourassa*, 2008; *Truitt Wiensz*, 2012; *Zawada*, 2015; *Dueck*, 2017; *Kocifaj*, 2018], Gauss-Seidel iterations [*Herman*, 1994**b**; *Loughman*, 2015; *Eluszkiewicz*, 2017], source integration for the first order of scattering [*Walter*, 2004, 2005, 2006; *Doicu*, 2009**c**], combined differential-integral approach [*Rozanov A*, 2000, 2001, 2002], finite-difference and adding-doubling [*Griffioen*, 2000], invariant imbedding [*Bellman*, 1967], Eddington [*Unno*, 1976], Picard iteration [*Doicu*, 2009**d**], small-angle modification [*Efremenko*, 2013], and Markov chain [*Xu*, 2013]. Only

---

[3] www.cambridge.org/stamnes or www.rtatmocn.com (accessed June 12, 2020)

Monte Carlo models can simulate multiple scattering in true spherical geometry, while the other models can only offer corrections to the plane-parallel approach (pseudo-sphericity). The pseudo-spherical approach aims to deploy the numerical efficiency of plane-parallel codes to provide practical results of sufficient accuracy.

Some of these codes have been deployed in spherical RT model intercomparisons [*Herman*, 1995; *Caudill*, 1997; *Ivezić*, 1997; *Petropavlovskikh*, 2000; *Postylayakov*, 2003; *Loughman*, 2004]. Contrary to situation with plane-parallel models, for which accurate benchmark data are available for a variety of scenarios [*Emde*, 2015; *Chowdhary*, 2020; see also *Korkin*, 2017: p.306, Table 1, for earlier references], these papers on spherical-model intercomparisons do not report numbers.

In addition to the field of Earth science, other disciplines have seen active publishing of numerical solutions to the transport equation in spherical geometry. Examples include astrophysics [*Ivezić*, 1997], planetary science [*Xu*, 2013], and neutron transport [*Davison*, 1958: p.146, Chapter XI "The spherical harmonics method for spherical geometries"]. In the latter field, accurate numerical data [*Garcia*, 2020] is available but usually for isotropic scattering from an internal source. This is similar to the thermal RT regime in a spherical Earth atmosphere, which is outside the scope of the present paper.

In rare cases, numerical benchmark data are in fact available. The *A&K* [1978: p.143, Table I] paper reports intensity reflected from a spherical Rayleigh atmosphere, but results are limited to the principal plane. Soon after the initial *A&K* publication, *Kattawar* & *Adams* [1978: p.440, Table I] and *Kattawar* [1979: p.63, Table II] published results for aerosols with the Henyey-Greenstein phase functions (2 different asymmetry parameters g = 0.5 and 0.7, principal plane only) and with Mie scattering optical inputs (ratio of single to multiple scattering and brightness temperature), respectively. *Blättner* [1974: p.543, Table III] also reported ratios of results using second-order scattering and multiple scattering to first-order scattering values. *Wilson* & *Sen* [1980: p.409, Table I] report approximate numerical results for a spherical atmosphere over a Lambertian surface, with comparisons to those obtained by *Sobolev* [1975: p.231]. *Ding* & *Gordon* [1994] confirmed the hypothesis of *Adams* & *Kattawar* [1978] that the multiple-to-single scattering ratio remains "sufficiently close" for the plane-parallel and spherical atmospheres in the principal plane. They also found that their numerical simulations agree with those in *Adams* & *Kattawar* [1978] within 0.3% (p.7098). *Spurr* [2002: p.155, Table 1] reports results for relative azimuth 60°. However, his test case input depends on the LOWTRAN atmospheric parameters, and cannot be easily reproduced [*Spurr*, 2002: p.156, Section 6.1]. The results of *Postylaykov* [2004: p.310, Table 1] suffer from similar problem. *Zhuravleva* [2019: p.7, Table 2] report fluxes, which is not helpful for validation of solar-view dependency in backscatter intensity.

It is clear that our literature analysis confirms the need for additional publication of numerical benchmark results for spherical atmospheres. The next section explains the methodology for obtaining our benchmarks and provides estimations of their accuracy.

Methodology

Spherical Atmosphere in MYSTIC and VLIDORT
The libRadtran's Monte Carlo RT solver MYSTIC simulates various radiative quantities, e.g., radiances and irradiances, monochromatic or spectrally integrated. The observer position can be on a satellite, on the ground or in the atmosphere, e.g. on an airplane. Per default, all scattering orders are simulated. For

theoretical studies it is also possible to simulate individual scattering orders. The variance reduction technique [*Buras*, 2011] was turned on in all our simulations. Following *Emde* et al. [2015: p.12], we used 100M photons in the reported results. We configured other input parameters using the manual available from the libRadtran website. *Emde* & *Mayer* [2007: p.2261] and *Ockenfuß et al.* [2019: p.4] briefly discuss the MYSTIC spherical geometry, in which a photon is traced "backward" from the detector to the source. In those papers, MYSTIC was tested against measurements taken during solar eclipses in the years 2006 and 2017. MYSTIC also allows to define a 3D spherical atmosphere. This option has been used to interpret the Very Large Telescope (ESO VLT) polarimetric earthshine observations in 2011 [*Emde*, 2017].

For reflectance, *A&K* [1978] and MYSTIC define the solar-view geometry at TOA which is different from that of VLIDORT. This difference must be accounted for in the comparisons. We refer the reader to Appendix 1 for details of the TOA-BOA transformation of the solar-view geometry in the principal plane, and Appendix 2 in a general case. In addition, Appendix 3 describes an algorithm for computation of the relative azimuths located on the sunlit side of the Earth. This effect is included naturally in the full-spherical code. In addition to the Appendices, Table 1 contains numerical values of solar-view geometries used in this work: Table 1(a) – BOA VZA as a function of the TOA; Table 1(b) – same as (a) but for SZA and relative azimuth in the principal plane; Table 1(c) – same as (b) but away from the principal plane.

Note that a pseudo-spherical solver based on the RT code DISORT [*Dahlback*, 1991] is also available in libRadtran. We do not include it in our benchmarks, due to relatively high reported error, ~5%-20%, depending on the solar-view geometry [*Herman*, 1994: Abstract; *Caudill*, 1995: Abstract].
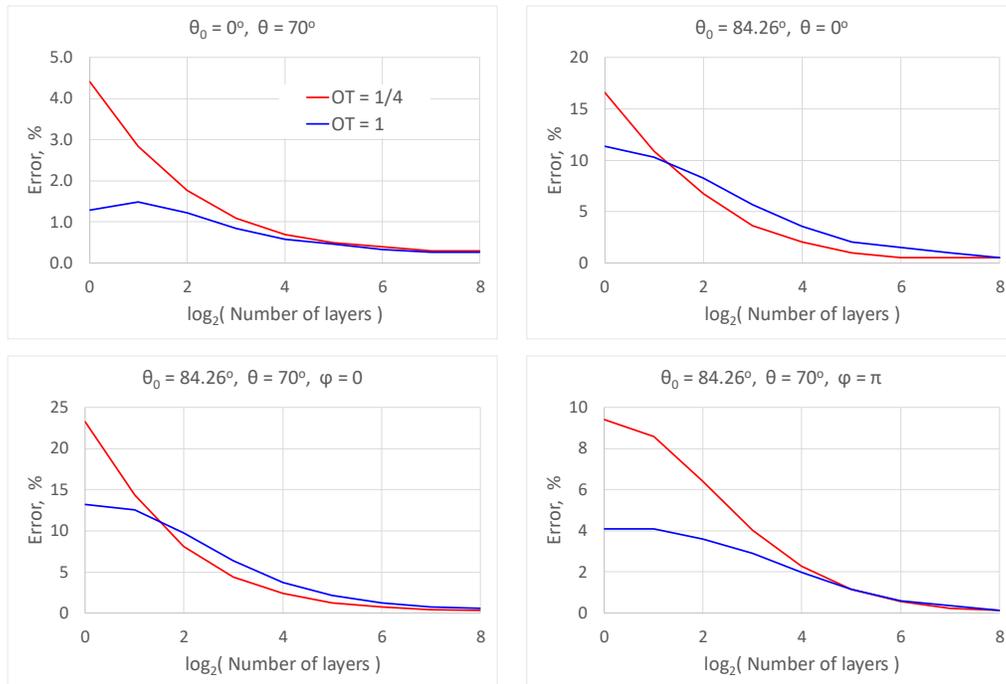
Fig.3: *Convergence of the single-scattering (SS) solution for different solar-view geometries (as indicated in panel titles) and optical thickness (OT) plotted against the number of layer elements. The scenario and the solar-view geometrical configuration are defined in A&K [1978: Table 1]. The SS subroutine was developed to account for the effect of sphericity in the plane-parallel RT code* IPOL [*Korkin*, 2019].

To increase accuracy of sphericity corrections within the framework of the multiple-scatter plane-parallel model, we adopt the following approach implemented in the new VLIDORT version 2.8.2. The single scattering (SS) radiation field is computed accurately in a spherical atmosphere using enough (~100) vertical layers (**Fig. 3**) to ensure a smooth variation of the solar and view angles along the LOS. For calculating multiple scattering (MS) radiation fields, the incident solar beam attenuation is calculated in a curved atmosphere as in the standard pseudo-spherical approximation. To allow for changes of geometry along the LOS, we run the MS computations twice: once for the TOA solar/view geometry configuration, and a second time with the BOA geometry. These two multiple scattering intensities (recall, we ignore polarization in this study) and a SS intensity, which is accurately known for a curved atmosphere, are used to build the upwelling intensity field in the atmosphere by source function integration, starting with the upwelling intensity at BOA. We now summarize this process.

At BOA, the VLIDORT calculation of upwelling intensity I_{surf} at the ground comprises two terms – the direct-bounce field I_{DB} from the accurate spherical SS code, and the diffuse-field multiple-scatter contribution I_{MB}:

$$I_{surf} = I_{DB} + I_{MB} \ . \tag{4}$$

Referring to the sketch in **Fig. 1**, when the LOS path traverses layer n in our curved atmosphere, the intensity I_{n-1} at the top of the layer is determined through source-function integration:

$$I_{n-1} = T_n I_n + S_n + M_n \ . \tag{5}$$

Here, the radiation field at layer bottom is I_n and T_n is the LOS transmittance. Terms S_n and M_n are the integrated SS and MS layer source terms respectively. Equation (5) is applied recursively along the LOS, starting with the BOA value I_{surf}, Eq.(4), at BOA and ending with the TOA radiation field I_0 at TOA.

The SS calculation based on the BOA geometrical configuration will deliver both the SS source term as well as the LOS transmittances T_n and S_n, along with the direct-bounce intensity at the surface I_{DB}; as noted already, this calculation is accurate for spherical geometry. The total recursively developed TOA field is then given by

$$I_0 = (I_{DB} + I_{MB})C_N + \sum_{n=1}^{N}(S_n + M_n)C_{n-1}, \ \ C_{n>0} = \prod_{k=1}^{n}T_k, \ C_0 = 1 \ . \tag{6}$$

The cumulative LOS transmittances are $\{C_n\}$, $n = 0, 1, ... N$. Here, N is the total number of layers.

The terms $\{M_n\}$, n= 1, …N are obtained as follows. The modified VLIDORT call will now supply I_{MB} (for the BOA-geometry configuration) and two sets $\{M_n^{(BOA)}\}$ and $\{M_n^{(TOA)}\}$ of multiple-scatter layer source terms from the two calculations with BOA and TOA geometries respectively. Next, these two sets of MS source terms are linearly interpolated against μ = cos(VZA) to find the changing value of M_n for each layer on the way from BOA to TOA. Although it is also possible to do this interpolation against μ_0 = cos(SZA) the interpolation against μ is free from ambiguities.

8

It should be noted that the diffuse-scattering surface intensity I_{MB} and the two sets of layer multiple-scattering source terms used in the source function integration are final values, after application of the cosine-azimuth summation of Fourier components of the intensity field.

We call this VLIDORT modification a "2-point sphericity correction". This correction is more accurate compared to the previous pseudo spherical corrections that have been considered in LIDORT and VLIDORT [*Spurr*, 2002; 2004; 2019]. The accuracy of the MS source term determination can be improved further by calling VLIDORT with 3 geometries, at BOA, TOA and one other pre-specified point along the LOS - this would be a "3-point sphericity correction". An even better accuracy could be obtained by calling VLIDORT with a whole series of geometrical configurations at every boundary level between BOA and TOA (i.e., "multipoint sphericity correction"). Obviously the 2-point correction is the fastest to implement.   Here we confine our attention to Rayleigh atmosphere, and consider only the 2-point corrections for VLIDORT in our comparisons with MYSTIC.

Accuracy of the results

MYSTIC is used in this paper as a baseline for our benchmarks. We have checked its convergence using the 3σ-rule (99.7% confidence) that estimates the relative accuracy of the Monte Carlo code as

$$I_{MC} = \tilde{I}_{MC} \pm 3\sigma,$$ (7)

where the mean intensity, $\tilde{I}_{MC}$, and the standard deviation, σ, are outputs from MYSTIC. We define the relative accuracy of the MC simulations according to

$$\varepsilon_{MC} = \frac{3\sigma}{\tilde{I}_{MC}} 100\% .$$ (8)

Following the recommendations in *Emde* [2015: p.12], we used 100M photons for the computations.

Table 2 gives the maximum and average errors over all solar-view geometries for two optical depths, separately for single and multiple scattering, and according to the abovementioned criteria. The table shows with confidence that MYSTIC converges within a 0.1% error.

Table 2: Monte Carlo convergence rate, in %, for single (SS) and multiple (MS) scattering modes, Eq.(8)

τ	Scattering	max	average
0.25	SS	0.06	0.04
0.25	MS	0.08	0.05
1.0	SS	0.06	0.03
1.0	MS	0.06	0.03

The accuracy of VLIDORT depends on three conditions: (1) a convergence criterion for the number of azimuthal (Fourier) expansion moments needed to compute the solution to a certain level accuracy; (2) the number of polar discrete ordinates (quadrature streams) used to solve the plane-parallel integro-differential RT equations in each layer; and (3) for a spherical atmosphere, the number of layers needed to account for smooth change of the solar-view geometry along the LOS (**Fig.3**). For the pure Rayleigh scattering case, there are no Fourier convergence or discrete ordinates issues – the 3 azimuthal (Fourier) components were computed using 8 discrete ordinates in each polar hemisphere (16 streams in total).

To ensure a smooth change of the solar-view geometry along the LOS, we executed VLIDORT with 100 layers and used control run with only 50 layers to ensure that the numerical uncertainty of this parameterization did not exceed 0.1%.

A&K do not provide explicit values of the standard deviation in their tabulated Monte Carlo results. However, they estimate the accuracy of their simulations for the *plane-parallel* case as follows (p.151). In SS the reciprocity principle, Eq.(3), is obeyed to within 3 significant digits; in MS – within 3%. For spherical atmospheres, they also provide SS numbers to 3 digits, which yields up to 0.3% (0.1% on average) and 0.5% (0.2% on average) for tau = 0.25 and 1.0, respectively, assuming that the round-off error dominates. For spherical geometry, A&K provide the SS/MS ratios using only 2 digits. Based on their accuracy estimations in the plane-parallel case, we set their relative accuracy for MS in spherical geometry to be 3%. It is worth noting that *Ding & Gordon* [1994: p.7098] agreed with A&K to within 0.3%.

Finally, before running the spherical examples, we checked VLIDORT and MYSTIC for consistency in inputs and accuracy in output through use of the A&K plane-parallel scenario. In all the plane-parallel cases, VLIDORT and MYSTIC results agreed with those from A&K at ~2% or better, and between each other at 0.1% or better. Both these deviations are close to what we expect, given the accuracy of the A&K tables, the MYSTIC standard deviation, and the VLIDORT number of streams. In the next section, we report on numerical results suitable for benchmarking spherical RT codes.

Numerical Results and Discussion

Following A&K, we consider the diffuse upwelling reflectance from a spherical conservative Rayleigh scattering atmosphere of optical thicknesses τ=0.25 and 1 over a black surface. Polarization and ray bending due to refraction are ignored. For SS, A&K report results to 3 significant digits, which is accurate enough for practical needs, but insufficiently precise for numerical tests aiming at an error level of 0.1%. For MS their results are less accurate: only 2 digits for the SS/MS scattering ratios. Therefore, we have reproduced their results with higher accuracy to provide a) 5 digits for both SS and MS, of which the latter suffers from round-off error; and b) absolute values for MS, instead of ratios.

Our results are grouped in Tables 3 and 4 for optical thickness 0.25 and 1.0. In each table, sections (a) and (b) correspond to SS and MS, respectively. We keep the appearance of our tables close to that for original tables by A&K. In Table 3a (τ=0.25, SS) the columns from left to right show: VZA at TOA, original results by A&K (except in exponential format), MYSTIC results, VLIDORT results, relative deviation of the A&K results vs. MYSTIC, relative deviation of VLIDORT results vs. MYSTIC. Tables 1(a) & (b) contain the solar-view geometry at BOA as input for VLIDORT. The VLIDORT's VZA at TOA is limited by the critical angle 79.9° (see the note in the Introduction). The solar (SZA) and azimuth (φ) angles at TOA go from top to bottom in grey fields in the sequence defined by A&K. For SS at OT=0.25, the maximum and average deviations of the A&K results from MYSTIC turned out to be 0.32% and 0.11%, respectively (indicated in color at the bottom of the table). The same quantities for VLIDORT are 0.05% and 0.02%.

The TOA solar-view geometry in Table 3b (OT=0.25, **MS**) is organized as in Table 3a, but the sequence of columns is slightly different: VZA at TOA (left-most entry), SS by A&K, SS/MS ratio from A&K. This ratio is followed by absolute values of the MS not indicated in the original tables. The four columns on the right are the same as those in Table 3(a). For MS at τ=0.25, the maximum and average deviations of the

A&K results from MYSTIC turned out to be 4.7% and 1.2%, respectively. The same quantities for VLIDORT are 0.5% and 0.3%.

Tables 4 (a)(b) are identical to Tables 3 (a)(b), respectively, but shows results for **OT = 1**. For SS (Table 4a) the maximum and average deviations of the A&K results from MYSTIC were 0.72% and 0.17%, respectively. The same quantities for VLIDORT were 0.07% and 0.02%. For multiple scattering (Table 4b) those numbers are 5.6% and 1.4% (A&K), and 0.37% and 0.11% (VLIDORT).

Tables 5 (OT=0.25) and 6 (OT=1) contain **new results** for configurations away from the principal plane for SS (a) and MS (b) scattering modes. The sequence of relative azimuths is φ = 45°, 90°, 135°. In all the tables, the columns from left to right indicate the TOA VZA, followed by MYSTIC, VLIDORT, and percentile deviations of the two model results. At the bottom of each table, we record the maximum and average deviations computed over all solar-view geometries for a given OT and scattering mode.

Table 7 combines all the deviations together; this table should be read alongside Table 2 (accuracy of MYSTIC).

Table 7: Maximum and average deviations for MYSTIC and VLIDORT, in %, for single (SS) and multiple (MS) scattering modes computed over all solar-view geometries off the principal plane (new benchmark results).

Scattering mode:	Single scattering		Multiple scattering	
τ	maximum	average	maximum	average
0.25	0.05	0.02	0.69	0.39
1.0	0.09	0.02	0.29	0.12

Summary

The need for accurate spherical RT (O-RT) codes, e.g., for remote sensing of the Earth's atmosphere from a geostationary orbit at dusk and dawn or Lagrange L1 orbit or remote sensing of Polar regions, has been growing fast, along with the requirement for comprehensive accurate benchmarks. In this paper, we have reproduced and extended results from *Adams & Kattawar* [1978] (A&K) for monochromatic solar light reflected from the top of the Earth's spherical atmosphere. In contrast to graphical figures frequently published in the literature, our numerical results are suitable for accurate benchmarking of the O-RT codes.

Our Tables 3-6 report numerical results for unpolarized light reflected from the top of a Rayleigh scattering atmosphere over a black surface, for two optical thicknesses (0.25 and 1.0), for both single and multiple scattering, in and out of the principal plane using two state-of-the art RT codes: libRadtran's MYSTIC (Monte Carlo) and VLIDORT (discrete ordinates). The two codes agreed perfectly (within 0.1%) for single scattering and within 0.7% (0.4% on average) for multiple scattering (Table 7).

However, this paper only partially fills the gap in O-RT benchmarking. Benchmark results for polarization, transmitted radiation, limb observations, reflecting surface, aerosol and absorption profiles, high cirrus clouds, and refraction among other effects are yet to be generated and tested.

Acknowledgments

References

1. Adams C.N., Kattawar G.W., 1978: Radiative transfer in spherical shell atmospheres. I. Rayleigh scattering, Icarus 35, 139-151;
2. Belikov Yu., Romanovsky Yu., Nikolashvili Sh., and Paradze R., 2000: Numerical model of scattering radiation in the Earth atmosphere for scientific investigations and applications, Phys. Chem. Earth (B), 25(5-6), 427-430.
3. Bellman R, Kagiwada H, and Kalaba R, 1967: Invariant imbedding and radiative transfer in spherical shells, J. Comp. Phys., 2, 245-256;
4. Bellman R, Kagiwada H, Kalaba R, and Ueno S, 1969: Diffuse reflection of solar rays by a spherical shell atmosphere, Icarus, 11, 417-423;
5. Blättner W.G., Horak H.G., Collins D.G., and Wells M.B., 1974: Monte Carlo studies of the sky radiance at twilight, Applied Optics, 13(3), 534-546;
6. Bourassa AE, Degenstein DA, and Llewellyn EJ, 2008: SASKTRAN: A spherical geometry radiative transfer code for efficient estimation of limb scattering sunlight, J. Quant. Spectrosc. Radiat, Transfer 109, 52–73;
7. Buehler SA, Mendrok J, Eriksson P, Perrin A, Larsson R, and Lemke O, 2018: ARTS, the atmospheric radiative transfer simulator — version 2.2, the planetary toolbox edition, Geosci. Model Dev., 11(4), 1537–1556;
8. Buras R, and Mayer B, 2011: Efficient unbiased variance reduction techniques for Monte Carlo simulations of radiative transfer in cloudy atmospheres: The solution, J. Quant. Spectrosc. Radiat, Transfer 112, 434-447;
9. Caudill T.R., Flittner D.E., Herman B.M., Torres O., and McPeters R.D., 1997: Evaluation of the pseudo-spherical approximation for backscattered ultraviolet radiances and ozone retrieval, J. Geophys. Res., 102, D3, 3881-3890;
10. Chowdhary J., Zhai P.-W., Xu F., Frouin R., and Ramon D., 2020: Testbed results for scalar and vector radiative transfer computations of light in atmopshere-ocean systems, J. Quant. Spectrosc. Radiat, Transfer 242, 106717;
11. Collins D.G., Blattner W.G., Wells M.B., and Horak H.G., 1972: Backward Monte Carlo calculations of the Polarization characteristics of the radiation emerging from spherical-shell atmospheres, Applied Optics, 11(11), 2684-2696.
12. Dahlback A., and Stamnes K., 1991: A new spherical model for computing the radiation field available for photolysis and heating at twilight, Planet Space Sci., 39(5), 671-683;
13. Davis C., Emde C., and Harwood R., 2005: A 3-D polarized reversed Monte Carlo radiative transfer model for millimeter and submillimeter passive remote sensing in cloudy atmospheres, IEEE Trans. Geosci. Rem. Sens., 43(5), 1096-1101;
14. Davison B., 1958: Neutron transport theory, Oxford University Press;
15. Ding K., and Gordon H.R., 1994: Atmospheric correction of ocean-color sensors: effects of the Earth's curvature, Appl. Opt. 33(30), 7096-7106;
16. Doicu A, Trautmann T, 2009a: Discrete-ordinate method with matrix exponential for a pseudospherical atmosphere: Scalar case, J. Quant. Spectrosc. Radiat, Transfer 110, 146–158.

17. Doicu A, Trautmann T, 2009b: Discrete-ordinate method with matrix exponential for a pseudospherical atmosphere: Vector case, J. Quant. Spectrosc. Radiat, Transfer 110, 159–172.
18. Doicu A, Trautmann T, 2009c: Adjoint problem of radiative transfer for a pseudo-spherical atmosphere and general viewing geometries, J. Quant. Spectrosc. Radiat, Transfer 110, 464–476;
19. Doicu A, Trautmann T, 2009d: Picard iteration methods for a spherical atmosphere, J. Quant. Spectrosc. Radiat, Transfer 110, 1851–1863.
20. Dubovik O., et al., 2019: Polarimetric remote sensing of atmospheric aerosols: Instruments, methodologies, results, and perspectives, J. Quant. Spectrosc. Radiat, Transfer 224, 474-511;
21. Dueck SRF, Bourassa AE, and Degenstein D, 2017: An efficient algorithm for polarization in the SASKTRAN radiative transfer framework, J. Quant. Spectrosc. Radiat, Transfer 199, 1–11
22. Efremenko DS, Doicu A, Loyola D, and Trautmann T., 2013: Small-angle modification of the radiative transfer equation for a pseudo-spherical atmosphere, Journal of Quantitative Spectroscopy and Radiative Transfer 114, 82–90;
23. Eluszkiewicz J, Uymin G., Flittner D., Cady-Pereira K., Malwer E, Henderson J, Moncet J-L, Nehrkorn T, and Wolff M, 2017: A fast code for channel limb radiances with gas absorption and scattering in a spherical atmosphere, J. Quant. Spectrosc. Rad. Trans. 193, 31-39;
24. Emde C., Buehler S.A., Davis C., Eriksson P., Sreerekha T.R., and Teichmann C., 2004: A polarized discrete ordinate scattering model for simulations of limb and nadir long-wave measurements in 1-D/3-D spherical atmosphere, J. Geoph. Res., 109, D24207;
25. Emde C, and Mayer B, 2007: Simulation of solar radiation during a total solar eclipse: a challenge for radiative transfer, Atmos. Chem. Phys., 7. 2259-2270;
26. Emde C, Barlakas V, Cornet C, Evans F, Korkin S, Ota Y, Labonnote LC, Lyapustin A, Macke A, Mayer B, Wendisch M, 2015: IPRT polarized radiative transfer model intercomparison project – Phase A, Journal of Quantitative Spectroscopy and Radiative Transfer 164, 8–36.
27. Emde C, Buras-Schnell R, Kylling A, Mayer B, Gasteiger J, Hamann U, Kylling J, Richter B, Pause C, Dowling T, and Bugliaro L, 2016: The libRadtran software package for radiative transfer calculations (version 2.0.1), Geoscientific Model Development 9(5), 1647-1672;
28. Emde C., Buras R., Sterzik M., and Bagnulo S., 2017: Influence of aerosols, clouds, and sunglint on polarization spectra of Earthshine, Astron. Astrophys., 605(A2);
29. Eriksson P, Buehler SA, Davis CP, Emde C, and Lemke O, 2011: ARTS, the atmospheric radiative transfer simulator, version 2, Journal of Quantitative Spectroscopy and Radiative Transfer 112, 1551-1558;
30. Garcia R.D.M., and Siewert C., 2020: A numerically stable spherical harmonics solution for the neutron transport equation in a spherical shell, Journal of Quantitative Spectroscopy and Radiative Transfer 405, 109139;
31. Gratiy SL, Levin DA, Walker AC, 2010a: Rassvet: Backward Monte Carlo radiative transfer in spherical-shell planetary atmospheres, Icarus 206, 366-379;
32. Gratiy SL, Walker AC, Levin DA, Goldstein DB, Varghese PL, Trafton LM, and Moore CH, 2010b: Multi-wavelength simulations of atmospheric radiation from Io with a 3-D spherical-shell backward Monte Carlo radiative transfer model, Icarus 207, 394-408;
33. Griffioen E, and Oikarinen L, 2000: LIMBTRAN: a pseudo three dimensional radiative transfer model for the limb-viewing imager OSIRIS on the ODIN satellite, J. Geophys. Res., 105, 29717-29730, 2000.
34. Herman BM, Ben-David A, Thome JK, 1994: Numerical technique for solving the radiative transfer equation for spherical shell atmosphere, Applied Optics 33(9), 1760-1770;

35. Herman BM, Caudill T, Flittner D, and Liou K.-N., 1995a: Comments on "Solar heating rates: The importance of spherical geometry", J. Atmos. Sci. 52(3), 380-382;

36. Herman BM, Caudill TR, Flittner DE, Thome KJ, and Ben-David A, 1995b: Comparison of the Gauss-Seidel spherical polarized radiative transfer code with other radiative transfer codes, Applied Optics 34(21), 4563-4572;

37. He X, Stamnes K, Bai Y, Li W, and Wang D, 2018: Effects of Earth curvature on atmospheric correction for ocean color remote sensing, Remote Sensing of Environment 209, 118-133;

38. Holben B.N., Eck T.F., Slutsker I., Tanré D., Buis J.P., Setzer A., Vermote E., Reagan J.A., Kaufman Y.J., Nakajima T., Lavenu F., Jankowiak I., and Smirnov A., 1998: AERONET-A Federated instrument Network and Data Archive for Aerosol Characterization, Rem. Sens. Env. 66, 1–16;

39. Ivezić Ž., Groenwegen M.A.T., Men'shchikov A., and Szczerba R., 1997: Benchmark problems for dust radiative transfer, Mon. Not. R. Astron. Soc. 291, 121-124;

40. Kalkofen W. (Ed), 1984: Methods in radiative transfer, Cambridge University Press;

41. Kattawar GW, Adams CN, 1978: Radiative transfer in spherical shell atmospheres. II. Asymmetric phase function, Icarus 35, 436-449;

42. Kattawar GW, 1979: Radiative transfer in spherical shell atmosphere. III. Application to Venus, Icarus 40, 60-66;

43. Kocifaj M, 2018: Multiple scattering contribution to the diffuse light of a night sky: A model which embraces all orders of scattering, J. Quant. Spectrosc. Rad. Trans., 206, 260-272;

44. Korkin S, Lyapustin A, Sinyuk A, Holben B, and Kokhanovsky A, 2017: Vector radiative transfer code SORD: performance analysis and quick start guide, Journal of Quantitative Spectroscopy and Radiative Transfer 200, 295-310.

45. Korkin S and Lyapustin A, 2019: Matrix exponential in C/C++ version of vector radiative transfer code IPOL, Journal of Quantitative Spectroscopy and Radiative Transfer 227, 106-110.

46. Kylling A., Stamnes K., and Tsay S.-C., 1995: A reliable and efficient two-stream algorithm for spherical radiative transfer: Documentation of accuracy in realistic layered media, J. Atmos. Chem. 21, 115-50;

47. Laszlo I, Stamnes K, Wiscombe W, and Tsay S-C, 2017: The discrete ordinate algorithm, DISORT for radiative transfer, in Light Scattering Reviews 11, Springer, Ed. Kokhanovsky A, 3-65;

48. Lenoble J., and Sekera Z., 1961: Equation of radiative transfer in a planetary spherical atmosphere, Proc. Nat. Acad. Sci. USA 47, 372-378;

49. Lenoble J. (Ed.), 1985: Radiative transfer in scattering and absorbing atmospheres: standard computational procedures, A. Deepak Publishing, Hampton VA;

50. Lenoble J., 1993: Atmospheric radiative transfer, A. Deepak Publishing, Hampton VA;

51. Loughman R.P., Griffioen E., Oikarinen L., Postylyakov O.V., Rozanov A., Flittner D.E., and Rault D.F., 2004: Comparison of radiative transfer sunlight measurements, J. Geograph. Res. 109, D06303;

52. Loughman R, Flittnes D, Nyaku E, and Bhartia PK, 2015: Gauss–Seidel limb scattering (GSLS) radiative transfer model development in support of the Ozone Mapping and Profiler Suite (OMPS) limb profiler mission, Atmos. Chem. Phys., 15, 3007-3020;

53. Lyapustin A, Wang Y, Korkin S, and Huang D, 2018: MODIS collection 6 MAIAC algorithm, Atmos. Meas. Tech., 11, 5741-5765.

54. Marchuk G.I., Mikhailov G.A., Nazarliev M.N., Darbinjan R.A., Kargin B.A., and Elepov B.S., 1980: The Monte Carlo method in atmospheric optics, Berlin: Springer;

55. Mayer B, Seckmeyer G, and Kylling A, 1997: Systematic long-term comparison of spectral UV measurements and UVSPEC modeling results, J. Geophys. Res. 102, 8755–8767;

56. Mayer B., and Kylling A., 2005: Technical note: The libRadtran software package for radiative transfer calculations - description and examples of use, Atmos. Chem. Phys. 5, 1855-1877;

57. Mayer B., 2009: Radiative transfer in the cloudy atmosphere, European Physical Journal Conferences 1, 75-99;

58. McCartney E.J., 1976: Optics of the atmosphere. Scattering by molecules and particles, John Wiley & Sons, New York NY;

59. McLinden C.A., McConnell J.C., Griffioen E., and McElroy C.T., 2002: A vector radiative-transfer model for the Odin/OSIRIS project, Can. J. Phys. 80, 375 - 393;

60. Nataraj V, and Spurr RJD, 2007: A fast linearized pseudo-spherical two orders of scattering model to account for polarization in vertically inhomogeneous scattering-absorbing media, Journal of Quantitative Spectroscopy and Radiative Transfer 107, 263-293;

61. Natsuyama H.H., Ueno S., and Wang A.P., 1998: Terrestrial radiative transfer. Modeling, computation, and data analysis, Springer;

62. Oikarinen L., Sihvola E., and Kyrölä E., 1999: Multiple scattering radiance in limb-viewing geometry, J. Geophys. Res. 104 (D24), 31261-31274;

63. Ockenfuβ P., Emde C., Mayer B., and Bernhard G, 2019: Accurate 3D radiative transfer simulation of spectral solar irradiance during the total solar eclipse of August 21, 2017, Atmos. Chem. Phys. Discusss., 609;

64. Petropavlovskih I., Loughman R., DeLuisi J., and Herman B., 2000: A comparison of UV intensities calculated by spherical atmopshere radiation transfer codes: application to aerosol corrections, J. Geoph. Res., 105, D11, 14737-14746.

65. Postylyakov O.V., Oikarinen L., Kyrola W., 2003: Fine comparison of radiative transfer models for scattering limb simulation, Geoph. Res. Abs. 5, 05566;

66. Postylyakov OV, 2004a: Linearized vector radiative transfer model MCC++ for a spherical atmosphere, Journal of Quantitative Spectroscopy and Radiative Transfer 88, 297-317;

67. Postylyakov OV, 2004b: Radiative transfer model MCC++ with evaluation of weighting functions in spherical atmosphere for use in retrieval algorithms, Journal of Quantitative Spectroscopy and Radiative Transfer 34, 721-726;

68. Premuda M., Palazzi E., Ravegnani F., Bortoli D., Masieri S., and Giovanelli G., 2012: MOCRA: a Monte Carlo code for the simulation of radiative transfer in the atmosphere, Optics Express 20(7), 7973-7993.

69. Ramon D, Steinmetz F, Jolivet D, Compiegne M, and Frouin R, 2019: Modelling polarized radiative transfer in the ocean-atmosphere system with the GPU-accelerated SMART-G Monte Carlo code, Journal of Quantitative Spectroscopy and Radiative Transfer 222-223, 89-107;

70. Rozanov AV, Rozanov VV, Burrows JP, 2000: Combined differential-integral approach for the radiation field computation in spherical shell atmosphere: Nonlimb geometry, Journal of Geophysical Research 105(D18), 22937-22942;

71. Rozanov A, Rozanov V, and Burrows JP, 2001: A numerical radiative transfer model for a spherical planetary atmosphere: combined differential-integral approach involving the Picard iterative approximation, Journal of Quantitative Spectroscopy and Radiative Transfer 69, 491-512;

72. Rozanov A, Rozanov V, and Burrows JP, 2002: Evaluation of the combined differential-integral approach for limb viewing geometry, Adv. Space Res., 29(11), 1843-1848;

73. Rozanov VV, Buchwitz M, Eichmann K-U, de Beek R, Burrows JP, 2002: SCIATRAN - a new radiative transfer model for geophysical applications in the 240–2400 nm spectral region: the pseudo-spherical version, Adv. Space. Res, 29, 1831–1835;

74. Rozanov A, Rozanov V, Buchwitz M, Kokhanovsky A., and Burrows JP, 2005: SCIATRAN - a new radiative transfer model for geophysical applications in the 240–2400 nm spectral region, Adv. Space Res. 36, 1015 – 1019;

75. Rozanov V, Rozanov A, Kokhanovsky A, Burrows J, 2014: Radiative transfer through terrestrial atmosphere and ocean: Software package SCIATRAN, J. Quant. Spect. Rad. Trans. 133, 13-71.

76. Rozenberg G.V., 1966: Twilight. A study in atmospheric optics. Springer Science + Business Media;

77. Sen KK, and Wilson SJ, 1990: Radiative transfer in curved media, Singapore: World Scientific;

78. Sinyuk A., Holben B.N., Eck T.F., Giles D.M., Slutsker I., Korkin S., Schafer J.S., Smirnov A., Sorokin M., and Lyapustin A., 2020: The AERONET Version 3 aerosol retrieval algorithm, associated uncertainties and comparisons to Version 2, Atmos. Meas. Tech. Discuss., 474;

79. Smokty O.I., 1969: Multiple light scattering in the spherical planetary atmosphere, Pure Appl. Geophys. 72, 214-226;

80. Sobolev V.V., 1975: Light scattering in planetary atmospheres, Pergamon Press, Oxford;

81. Spada F, Krol MC, and Stammes P, 2006: McSCIA: application of the Equivalence Theorem in a Monte Carlo radiative transfer model for spherical shell atmospheres, Atmos. Chem. Phys. 6, 4823 - 4842;

82. Spurr RJD, 2002: Simultaneous derivation of intensities and weighting functions in a general pseudo-spherical discrete ordinate radiative transfer treatment, Journal of Quantitative Spectroscopy and Radiative Transfer 75, 129-175;

83. Spurr R.J.D., 2004: LIDORT V2PLUS: a comprehensive radiative transfer package for UV/VIS/NIR nadir remote sensing, Proc. SPIE 5235, 89-100;

84. Spurr R, and Christi M, 2019: The LIDORT and VLIDORT linearized scalar and vector discrete ordinate radiative transfer models: updates in the last 10 years, In: A. Kokhanovsky (Ed.), Springer Series in Light Scattering;

85. Stamnes K., Tsay S.C., Wiscombe W., Jayaweera K., 1988: Numerically stable algorithm for discrete-ordinate-method radiative transfer in multiple scattering and emitting layered media, Applied Optics, 27 (12), p.2502-2509;

86. Stamnes K, Thomas GE, and Stamnes J, 2017: Radiative transfer in the atmosphere and ocean, 2nd Edition, Cambridge University Press, Cambridge.

87. Truitt Wiensz J., Bourassa A.E., Lloyd N.D., Wiacek A., Martin R.V., and Degenstein D.A., 2012: Photon conservation in scattering by large ice crystals with the SASKTRAN radiative transfer model, Journal of Quantitative Spectroscopy and Radiative Transfer 113, 582-593;

88. Tzortziou M., Krotkov N., Cede A., Herman J.R., and Vasilkov A., 2008: A new technique for retrieval of tropospheric and stratospheric ozone profiles using sky radiance measurements at multiple view angles: Application to a Brewer spectrometer, J. Geophys. Res. 113, D06304;

89. Unno W, and Kondo M, 1976: The Eddington approximation generalized for radiative transfer in spherically symmetric systems. I. Basic method, Publ. Astron. Soc. Japan, 28, 347-354;

90. van Oss R.F., Spurr R.J.D., 2002: Fast and accurate 4 and 6 stream linearized discrete ordinate radiative transfer models for ozone profile retrieval, J. Quant. Spectrosc. Rad.Transf. 75, 177-220;

91. Walter HH, Landgraf J, Hasekamp OP, 2004: Linearization of pseudo-spherical vector radiative transfer model, Journal of Quantitative Spectroscopy and Radiative Transfer 85, 251-283;

92. Walter HH, and Landgraf J, 2005: Towards linearization of atmospheric radiative transfer in spherical geometry, Journal of Quantitative Spectroscopy and Radiative Transfer 95, 175-200;

93. Walter H.H., Landgraf J., Spada F., and Doicu A., 2006: Linearization of a radiative transfer model in spherical geometry, J. Geoph. Res. 111, D24304;

94. Wilson SJ, and Sen KK, 1980: Light scattering by an optically thin inhomogeneous, spherically-symmetric planetary atmosphere: Brightness at the zenith near the terminator, Astrophysics and Space Scince, 71, 405-410;

95. Xu F, West RA, Davis AB, 2013: A hybrid method for modelling polarized radiative transfer in a spherical-shell planetary atmosphere, Journal of Quantitative Spectroscopy and Radiative Transfer 117, 59-70;

96. Zawada DJ, Dueck SR, Rieger LA, Bourassa AE, Lloyd ND, and Degenstein DA, 2015: High-resolution and Monte Carlo additions to the SASKTRAN radiative transfer model, Atmos. Meas. Tech. 8, 2609 - 2623;

97. Zhuravleva T., Nasrtdinov I., Chesnokova T., and Ptashnik I., 2019: Monte Carlo simulation of thermal radiative transfer in spatially inhomogeneous clouds taking into account the atmospheric sphericity, Journal of Quantitative Spectroscopy and Radiative Transfer 236, 106602.

Appendix 1: Transformation of the Solar-View Geometry from TOA to BOA in the Principal Plane

Here we derive the solar-view geometry at BOA from the one at TOA in the principal plane. VLIDORT uses the BOA geometry as the baseline, while A&K and MYSTIC use the TOA configuration.

Fig.4 shows several solar beam directions for a given LOS (view direction). The relative TOA azimuth, $\varphi_{TOA} = 0$, corresponds to forward scattering.
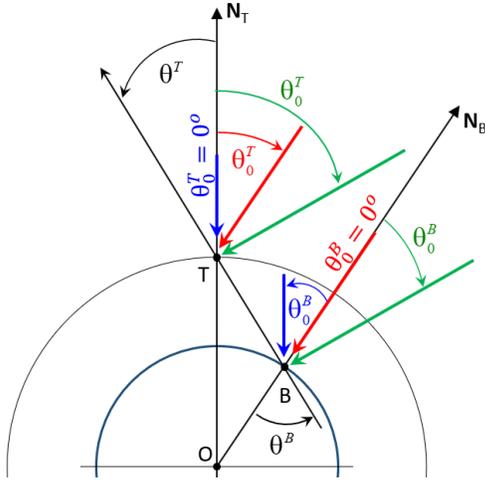
Fig.4(a): Different solar-view geometries in the principal plane 0-180. The outgoing view direction (black) is given, the solar direction varies (green, red - critical, blue). This image corresponds to $\varphi_{TOA} = 0$
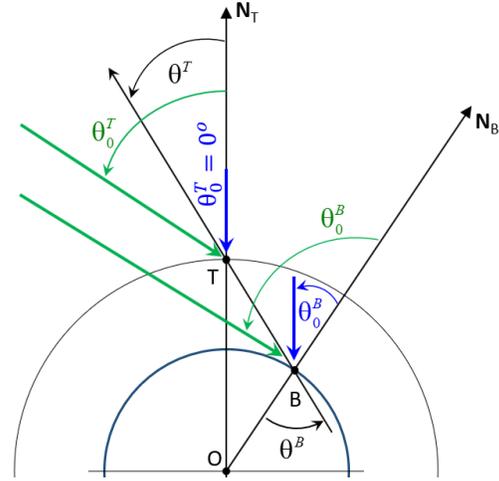
Fig.4(b): Same as Fig.4(a), except for $\varphi_{TOA} = 180$. There is no critical (red) solar beam direction in this case.

The TOA-to-BOA computation of the VZA at BOA uses the sine-rule relation, Eq.(1) We get the solar zenith angle at BOA depending on the TOA input as described below. We assume $\varphi_{BOA} = \varphi_{TOA}$ if the BOA azimuth is undefined.

Case 1 (Fig.4(a)): $\varphi_{TOA} = 0$. The "red" solar beam is a limiting case for the "green" one: $\theta_{0, BOA} = 0$, φ_{BOA} is not defined $\theta_{0,TOA}^{Critical} = \theta_{BOA} - \theta_{TOA}$ is a critical value. For $\theta_{0, TOA} < \theta_{0, TOA}^{Critical}$, the relative azimuths at TOA & BOA differ; otherwise, the azimuth is preserved. Both VZAs are known from the sine-rule relation, $\theta_{BOA} > \theta_{TOA}$. For the "green" solar beam: $\varphi_{BOA} = 0$; $\theta_{0, TOA} + \theta_{TOA} = \theta_{0, BOA} + \theta_{BOA}$. For the "blue" solar beam: $\theta_{0, TOA} < \theta_{0, TOA}^{Critical}$, $\varphi^{BOA} = 180$, $\theta_{0, TOA} + \theta_{TOA} = \theta_{BOA} - \theta_{0, BOA}$ - note the minus sign.

$\theta_{0, TOA} = 0$ falls under the "blue" case; also, this is the smallest possible $\theta_{0, TOA} = 0$ defines the largest possible $\theta_{0, BOA}$ (in the $\varphi_{BOA} = \pi$ half-plane) for any given VZA on TOA.

Case 2: $\varphi_{TOA} = 180$ (Fig.4(b)).

In this case, $\varphi_{BOA} = 180^{o}$ for any sun position. The BOA SZA is computed as

$$\theta_{0, BOA} = \theta_{0, TOA} + \theta_{BOA} - \theta_{TOA} .$$

However, there is a critical SZA at TOA for which the observed point is no longer irradiated by the Sun:

$$\theta_{0,\,BOA} = 90 = \theta_{0,\,TOA} + \theta_{BOA} - \theta_{TOA} \Rightarrow \theta_{0,\,TOA} = 90 + \theta_{TOA} - \theta_{0,\,TOA}\,.$$

The solar-view geometry at TOA and BOA used to reproduce the A&K results is listed in Table 1, with 2 significant digits after the decimal point. Appendix 3 below discusses the case of the Earth shadow.

Appendix 2: General Transformation of the Solar-View Geometry from BOA to TOA and vice versa

From Eq.(2) and the procedure outlined in Appendix 1, we see that some solar-view geometries at TOA have no corresponding configurations at BOA, thanks to the line of sight not hitting hit the Earth and/or the point of observation is in the Earth shadow. Therefore, in atmospheric and terrestrial applications, the solar-view geometry is often defined at BOA. In this Appendix 2 we provide equations to transform the solar-view geometry from BOA to TOA for arbitrary relative azimuth. After that, we "invert" the problem in order to compute input for VLIDORT (BOA) from the given TOA angles (input for A&K and MYSTIC). Fig.5 shows the geometry.
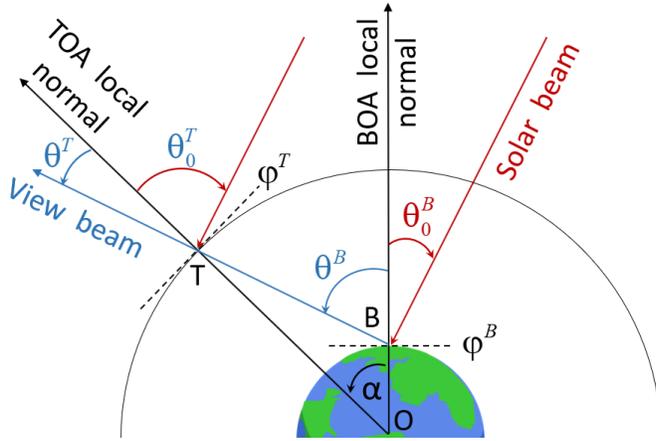
Fig.5: *The solar-view geometry, and TOA and BOA local normal vectors. Note, the scattering angle is the same at arbitrary point in atmosphere.*

From Eq.(2), one readily computes $\theta^B \geq \theta^T$. Further the angle, α, between the two local normal vectors at TOA and BOA is

$$\alpha = \theta_B - \theta_T\,, \tag{9}$$

The coordinates of the TOA local normal in the earth-centered coordinate system are

$$\mathbf{n}_T = \begin{bmatrix} \sin\alpha\cos\varphi_B & \sin\alpha\sin\varphi_B & \cos\alpha \end{bmatrix} \tag{10}$$

and the solar beam direction is

$$\mathbf{l}_0 = \begin{bmatrix} \sin\theta_{0,\,B} & 0 & -\cos\theta_{0,\,B} \end{bmatrix} \tag{11}$$

with respect to the BOA normal pointing towards the space (hence, $z_0 = -\cos\theta_{0,\,B} \leq 0$). The cosine of the solar angle at TOA comes from the dot product of Eqs. (10) and (11)

$$\cos(180 - \theta_{0,T}) = \mathbf{l}_0 \mathbf{n}_T = \sin\alpha \sin\theta_{0,B} \cos\varphi_B - \cos\alpha \cos\theta_{0,B} = -\cos\theta_{0,T} \tag{12}$$

Equality of the scattering angle, Θ, at TOA and BOA yields the TOA azimuth

$$\cos\Theta = -\cos\theta_B \cos\theta_{0,B} + \sin\theta_B \sin\theta_{0,B} \cos\varphi_B = -\cos\theta_T \cos\theta_{0,T} + \sin\theta_T \sin\theta_{0,T} \cos\varphi_T \ , \tag{13}$$

except for the case of normal irradiance of the TOA, $\cos\theta_{0,T} = 0$ in Eq.(12), when the azimuth at BOA is undefined, and also for the exact nadir observation situation, $\sin\theta_T = \sin\theta_B = 0$.

There is an inevitable loss of accuracy due to multiple trigonometric function results in $\varphi_T \neq 0$ or $\varphi_T \neq 180$ in the principal plane. If critical, the developer should consider the case of the observation in the principal plane separately (Appendix 1) or if-check φ_T to be "sufficiently close" to 0° or 180°.

If on the other hand the BOA geometry is to be computed from the TOA configuration, then one looks for $\theta_{0,B}$ and φ_B (recall, θ_B comes from Eq. (1)) from this system of Eqs. (12)-(13)

$$\begin{cases} \sin\alpha \sin\theta_{0,B} \cos\varphi_B - \cos\alpha \cos\theta_{0,B} = -\cos\theta_{0,T} \\ \sin\theta_B \sin\theta_{0,B} \cos\varphi_B - \cos\theta_B \cos\theta_{0,B} = \cos\Theta \end{cases} , \tag{14}$$

or in matrix form

$$\begin{bmatrix} -\sin\alpha & \cos\alpha \\ \sin\theta_B & -\cos\theta_B \end{bmatrix} \begin{bmatrix} \sin\theta_{0,B} \cos\varphi_B \\ \cos\theta_{0,B} \end{bmatrix} = \begin{bmatrix} \cos\theta_{0,T} \\ \cos\Theta \end{bmatrix} , \tag{15}$$

where singular matrix cases (e.g. for exact nadir observation) must be treated separately.

Appendix 3: Azimuthal Location of Points in the Earth Shadow

In this Appendix we derive equations to find the TOA azimuths that correspond to sunlit points at the surface level. Figures 6 (a) and (b), for pure Rayleigh scattering and scattering with some aerosol loading, respectively, show sudden drops of intensity when plotted against the TOA azimuth. This effect is captured by a true-spherical code such as MYSTIC. Fig.6(c) explains the effect: points A and B are always visible, while points E, D, and C disappear into the Earth shadow in that order when the LOS rotates from the forward scattering, $\varphi_{TOA} = 0$, to the backscattering, $\varphi_{TOA} = 180$, geometry.

From the right-angle triangle PEO, $PE^2 = R_E^2 - OE^2$; from the right-angle triangle SEO, $OE = SO \sin(\alpha)$; and the distance to the point of observation is

$$SP = SE - PE = SO \cos(\alpha) - \sqrt{R_E^2 - SO^2 \sin^2(\alpha)}$$

Using Heron's rule for the area of SPO

$$\Delta_{SPO} = \sqrt{p(p - R_E)(p - SO)(p - SP)} ,$$

where *p* is the semi-perimeter of SPO, we can derive the height of the SPO triangle:

$$PA = 2\Delta_{SPO} / SO .$$

From the triangles PAO and TAO we find that $AO = \sqrt{R_E^2 - PA^2}$ and $TA = AO/\tan(\theta_0)$, respectively. If TA < PA, the range of visible azimuths is defined from the right image of Fig.7 as

$$\varphi_{max} = 180^o - \phi = 180^o - \arccos(TA/PA).$$

Otherwise, all azimuths are visible from S and the given solar-view geometry. This includes the particular case of $\theta_0 \to 0^o$.
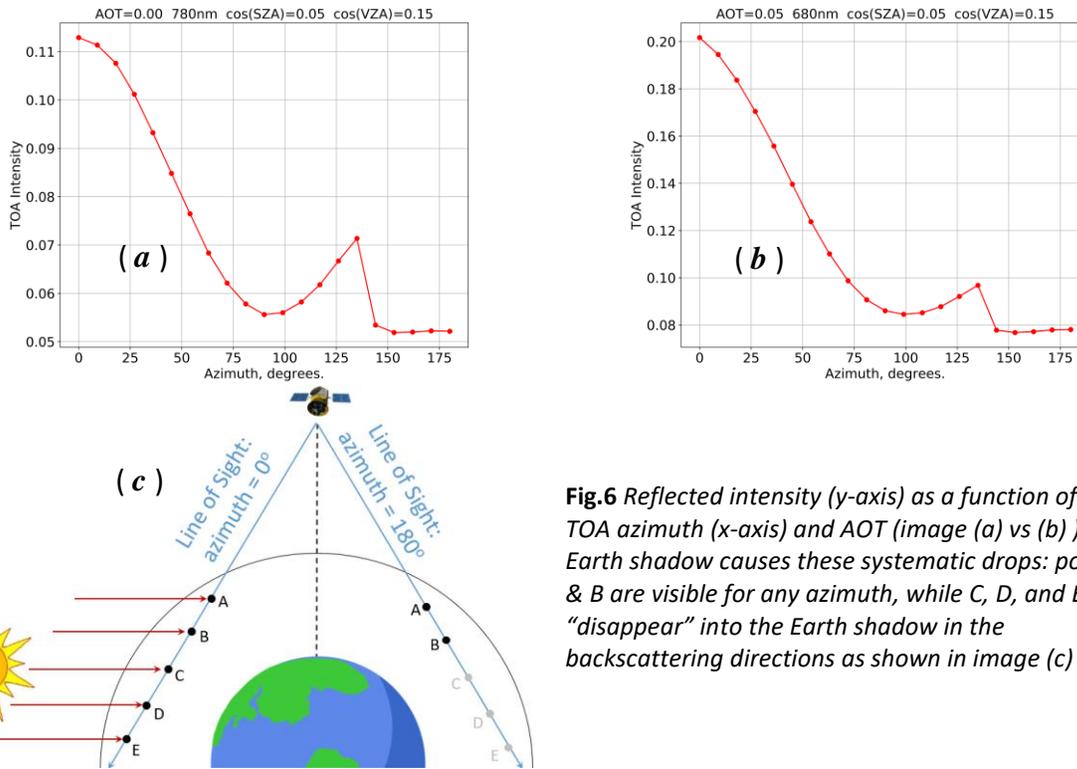
Fig.6 *Reflected intensity (y-axis) as a function of the TOA azimuth (x-axis) and AOT (image (a) vs (b)). The Earth shadow causes these systematic drops: points A & B are visible for any azimuth, while C, D, and E "disappear" into the Earth shadow in the backscattering directions as shown in image (c)*

Fig.7 shows the range of sunlit azimuths as 180° - φ, where φ values correspond to the TOA azimuths of those points in the Earth shadow. We suppose the satellite S, is located at a height SB above the ground and P is a point on the ground surface observed at scan angle α (μ is the cosine). The solar beam direction and the satellite nadir span an angle θ₀.
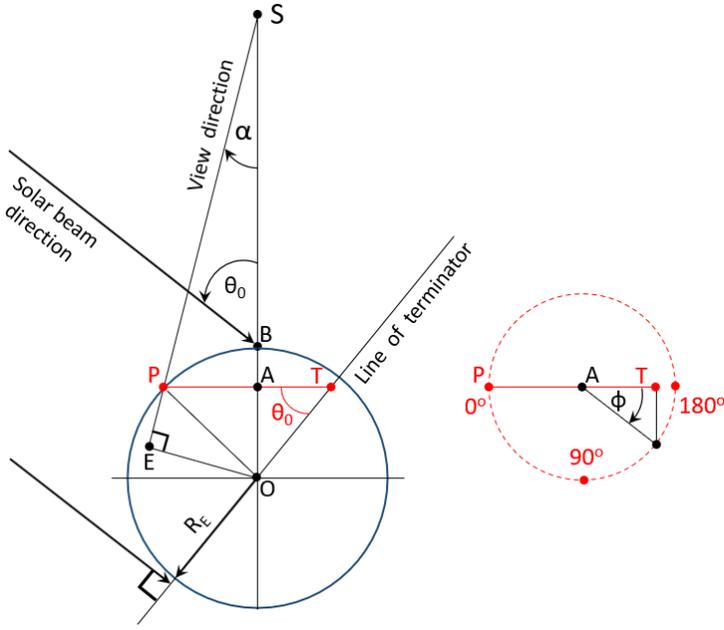
Fig.7: Geometrical sketch to define the range of the "sunlit azimuths"; R_E is the Earth radius.

Tables

Table 1(a): VZA at BOA as a function of VZA at TOA.

θ_TOA	θ_BOA
0	0.00
10	10.16
20	20.33
30	30.52
40	40.76
50	51.08
60	61.60
70	72.64

Table 1(b): Same as Table 1(a) except for SZA and relative azimuth in the principal plane.

# θ_TOA	θo_BOA	φ_BOA
#	θo_TOA = 0	φ_TOA
0	0	180
10	0.16	180
20	0.33	180
30	0.52	180
40	0.76	180
50	1.08	180
60	1.6	180
70	2.64	180
#	θo_TOA = 70.47	φ_TOA = 0
0	70.47	0
10	70.31	0
20	70.14	0
30	69.95	0
40	69.71	0
50	69.39	0
60	68.87	0
70	67.83	0

Table 1(b): Continued.

# θ_TOA	θo_BOA	φ_BOA
#	θo_TOA = 84.26	φ_TOA = 0
0	84.26	0
10	84.1	0
20	83.93	0
30	83.74	0
40	83.5	0
50	83.18	0
60	82.66	0
70	81.62	0
#	θo_TOA = 70.47	φ_TOA = 180
0	70.47	180
10	70.63	180
20	70.8	180
30	70.99	180
40	71.23	180
50	71.55	180
60	72.07	180
70	73.11	180
#	θo_TOA = 84.26	φ_TOA = 180
0	84.26	180
10	84.42	180
20	84.59	180
30	84.78	180
40	85.02	180
50	85.34	180
60	85.86	180
70	86.9	180

Table 1(c): Same as Table 1(b) but away from the principal plane.

# θ_TOA	θo_BOA	φ_BOA
#	θo_TOA = 70.47	φ_TOA = 45
0	70.47	45.00
10	70.36	45.04
20	70.24	45.08
30	70.10	45.13
40	69.93	45.19
50	69.71	45.28
60	69.35	45.41
70	68.62	45.70

Table 1(c): Continued.

# θ_TOA	θo_BOA	φ_BOA
#	θo_TOA = 84.26	φ_TOA = 45
0	84.26	45.00
10	84.15	45.01
20	84.03	45.02
30	83.89	45.04
40	83.72	45.06
50	83.49	45.08
60	83.13	45.12
70	82.40	45.22
#	θo_TOA = 70.47	φ_TOA = 90
0	70.47	90.00
10	70.47	90.06
20	70.47	90.12
30	70.47	90.18
40	70.47	90.27
50	70.47	90.38
60	70.48	90.57
70	70.49	90.94
#	θo_TOA = 84.26	φ_TOA = 90
0	84.26	90.00
10	84.26	90.02
20	84.26	90.03
30	84.26	90.05
40	84.26	90.08
50	84.26	90.11
60	84.26	90.16
70	84.27	90.27
#	θo_TOA = 70.47	φ_TOA = 135
0	70.47	135.00
10	70.58	135.04
20	70.70	135.08
30	70.84	135.13
40	71.01	135.19
50	71.24	135.27
60	71.60	135.39
70	72.35	135.62

Table 1(c): Continued.

# θ_TOA	θo_BOA	φ_BOA
#	θo_TOA = 84.26	φ_TOA = 135
0	84.26	135.00
10	84.37	135.01
20	84.49	135.02
30	84.63	135.04
40	84.80	135.05
50	85.03	135.07
60	85.39	135.10
70	86.13	135.16

Table 2: See in the text, page 9.

Tables 3-6: See below.

Table 3(a): Reproduced results by A&K for SS and OT=0.25. Columns (left to right) show: TOA VZA, original results by A&K (except in exponential format), MYSTIC (MC) results, VLIDORT (VL) results, relative deviation of the A&K results vs MYSTIC, relative deviation of VLIDORT results vs MYSTIC. Maximum and average errors are indicated below, sign of errors ignored.

# θ_TOA	A&K	MC	VL	|A&K vs MC| %	|VL vs MC| %
#		θo_TOA = 0	φ_TOA		
0	7.38E-02	7.3785E-02	7.3776E-02	0.02	0.01
10	7.37E-02	7.3678E-02	7.3669E-02	0.03	0.01
20	7.35E-02	7.3420E-02	7.3442E-02	0.11	0.03
30	7.34E-02	7.3416E-02	7.3393E-02	0.02	0.03
40	7.41E-02	7.4131E-02	7.4135E-02	0.04	0.01
50	7.68E-02	7.6828E-02	7.6827E-02	0.04	0.00
60	8.40E-02	8.3928E-02	8.3945E-02	0.09	0.02
70	1.02E-01	1.0171E-01	1.0172E-01	0.29	0.01
80	1.72E-01	1.7215E-01		0.09	
85	1.71E-01	1.7132E-01		0.19	
88	1.26E-01	1.2623E-01		0.18	
#		θo_TOA = 70.47	φ_TOA = 0		
0	3.33E-02	3.3331E-02	3.3331E-02	0.09	0.00
10	3.13E-02	3.1281E-02	3.1274E-02	0.06	0.02
20	3.18E-02	3.1804E-02	3.1804E-02	0.01	0.00
30	3.54E-02	3.5403E-02	3.5404E-02	0.01	0.00
40	4.30E-02	4.2963E-02	4.2979E-02	0.09	0.04
50	5.63E-02	5.6271E-02	5.6261E-02	0.05	0.02
60	7.92E-02	7.9092E-02	7.9117E-02	0.14	0.03
70	1.22E-01	1.2190E-01	1.2191E-01	0.08	0.01
80	2.54E-01	2.5377E-01		0.09	
85	2.94E-01	2.9408E-01		0.03	
88	2.33E-01	2.3252E-01		0.21	

Table 3(a): Continued.

# θ_TOA	A&K	MC	VL	|A&K vs MC| %	|VL vs MC| %
#		θo_TOA = 84.26	φ_TOA = 0		
0	1.93E-02	1.9258E-02	1.9261E-02	0.22	0.02
10	1.96E-02	1.9562E-02	1.9561E-02	0.20	0.00
20	2.17E-02	2.1662E-02	2.1674E-02	0.17	0.05
30	2.59E-02	2.5905E-02	2.5904E-02	0.02	0.00
40	3.29E-02	3.2888E-02	3.2892E-02	0.04	0.01
50	4.40E-02	4.3926E-02	4.3904E-02	0.17	0.05
60	6.21E-02	6.2019E-02	6.2043E-02	0.13	0.04
70	9.62E-02	9.6035E-02	9.6061E-02	0.17	0.03
80	2.10E-01	2.1001E-01		0.01	
85	2.79E-01	2.7884E-01		0.06	
88	2.39E-01	2.3945E-01		0.19	
#		θo_TOA = 70.47	φ_TOA = 180		
0	3.34E-02	3.3336E-02	3.3331E-02	0.19	0.01
10	3.78E-02	3.7731E-02	3.7734E-02	0.18	0.01
20	4.45E-02	4.4451E-02	4.4442E-02	0.11	0.02
30	5.37E-02	5.3653E-02	5.3649E-02	0.09	0.01
40	6.60E-02	6.5919E-02	6.5927E-02	0.12	0.01
50	8.27E-02	8.2609E-02	8.2604E-02	0.11	0.01
60	1.07E-01	1.0681E-01	1.0682E-01	0.18	0.01
70	1.47E-01	1.4714E-01	1.4713E-01	0.09	0.00
80	2.50E-01	2.5012E-01		0.05	
85	3.00E-01	2.9989E-01		0.04	
88	2.37E-01	2.3719E-01		0.08	

Table 3(a): Continued.

# θ_TOA	A&K	MC	VL	|A&K vs MC| %	|VL vs MC| %
#		θo_TOA = 84.26	φ_TOA = 180		
0	1.93E-02	1.9258E-02	1.9261E-02	0.22	0.02
10	2.07E-02	2.0650E-02	2.0645E-02	0.24	0.02
20	2.38E-02	2.3725E-02	2.3719E-02	0.32	0.02
30	2.87E-02	2.8646E-02	2.8649E-02	0.19	0.01
40	3.59E-02	3.5818E-02	3.5821E-02	0.23	0.01
50	4.61E-02	4.6124E-02	4.6138E-02	0.05	0.03
60	6.15E-02	6.1527E-02	6.1530E-02	0.04	0.01
70	8.72E-02	8.7254E-02	8.7245E-02	0.06	0.01
80	1.41E-01	1.4091E-01		0.07	
85	2.00E-01	1.9995E-01		0.03	
88	2.31E-01	2.3099E-01		0.00	
MAX %				0.32	0.05
AVER %				0.11	0.02

Table 3(b): Similar to Table 3(a) except for MS. Columns (left to right) show: TOA VZA, SS from A&K, SS/MS ratio from A&K, absolute values of the MS (not indicated in the original A&K tables). The four right-most columns are the same as those in Table 3(a).

# θ_TOA	A&K SS	A&K SS/MS %	A&K MS	MC	VL	|A&K vs MC| %	|VL vs MC| %
#			$\theta o\_TOA = 0$	φ_TOA			
0	7.38E-02	82	9.00E-02	9.0710E-02	9.0779E-02	0.78	0.08
10	7.37E-02	81	9.10E-02	9.0930E-02	9.0985E-02	0.06	0.06
20	7.35E-02	80	9.19E-02	9.1661E-02	9.1731E-02	0.23	0.08
30	7.34E-02	80	9.18E-02	9.3326E-02	9.3439E-02	1.69	0.12
40	7.41E-02	76	9.75E-02	9.6852E-02	9.6981E-02	0.67	0.13
50	7.68E-02	74	1.04E-01	1.0391E-01	1.0404E-01	0.12	0.13
60	8.40E-02	70	1.20E-01	1.1806E-01	1.1828E-01	1.64	0.19
70	1.02E-01	67	1.52E-01	1.4869E-01	1.4912E-01	2.39	0.29
80	1.72E-01	67	2.57E-01	2.5879E-01		0.80	
85	1.71E-01	67	2.55E-01	2.5168E-01		1.41	
88	1.26E-01	72	1.75E-01	1.7773E-01		1.54	
#			$\theta o\_TOA = 70.47$	φ_TOA = 0			
0	3.33E-02	69	4.83E-02	4.8711E-02	4.8822E-02	0.92	0.23
10	3.13E-02	68	4.60E-02	4.6932E-02	4.7052E-02	1.92	0.26
20	3.18E-02	64	4.97E-02	4.8469E-02	4.8578E-02	2.52	0.23
30	3.54E-02	64	5.53E-02	5.3883E-02	5.4008E-02	2.65	0.23
40	4.30E-02	67	6.42E-02	6.4359E-02	6.4517E-02	0.28	0.24
50	5.63E-02	70	8.04E-02	8.2185E-02	8.2371E-02	2.14	0.23
60	7.92E-02	71	1.12E-01	1.1238E-01	1.1267E-01	0.74	0.26
70	1.22E-01	73	1.67E-01	1.6855E-01	1.6912E-01	0.84	0.34
80	2.54E-01	75	3.39E-01	3.4233E-01		1.07	
85	2.94E-01	78	3.77E-01	3.7844E-01		0.40	
88	2.33E-01	81	2.88E-01	2.8599E-01		0.58	

Table 3(b): Continued.

# θ_TOA	A&K SS	A&K SS/MS %	A&K MS	MC	VL	|A&K vs MC| %	|VL vs MC| %
#			θo_TOA = 84.26	φ_TOA = 0			
0	1.93E-02	68	2.84E-02	2.8873E-02	2.9016E-02	1.70	0.49
10	1.96E-02	67	2.93E-02	2.9437E-02	2.9576E-02	0.62	0.47
20	2.17E-02	67	3.24E-02	3.2263E-02	3.2412E-02	0.39	0.46
30	2.59E-02	72	3.60E-02	3.7741E-02	3.7915E-02	4.69	0.46
40	3.29E-02	70	4.70E-02	4.6720E-02	4.6928E-02	0.60	0.45
50	4.40E-02	74	5.95E-02	6.0849E-02	6.1098E-02	2.28	0.41
60	6.21E-02	74	8.39E-02	8.4091E-02	8.4469E-02	0.20	0.45
70	9.62E-02	76	1.27E-01	1.2777E-01	1.2842E-01	0.93	0.51
80	2.10E-01	77	2.73E-01	2.7563E-01		1.05	
85	2.79E-01	82	3.40E-01	3.4411E-01		1.12	
88	2.39E-01	86	2.78E-01	2.7977E-01		0.66	
#			θo_TOA = 70.47	φ_TOA = 180			
0	3.34E-02	67	4.99E-02	4.8722E-02	4.8823E-02	2.32	0.21
10	3.78E-02	69	5.48E-02	5.3488E-02	5.3607E-02	2.42	0.22
20	4.45E-02	75	5.93E-02	6.1268E-02	6.1394E-02	3.16	0.21
30	5.37E-02	76	7.07E-02	7.2323E-02	7.2491E-02	2.30	0.23
40	6.60E-02	76	8.68E-02	8.7534E-02	8.7713E-02	0.79	0.20
50	8.27E-02	77	1.07E-01	1.0866E-01	1.0889E-01	1.16	0.21
60	1.07E-01	76	1.41E-01	1.3996E-01	1.4027E-01	0.59	0.22
70	1.47E-01	76	1.93E-01	1.9287E-01	1.9339E-01	0.29	0.27
80	2.50E-01	76	3.29E-01	3.3037E-01		0.43	
85	3.00E-01	79	3.80E-01	3.7920E-01		0.14	
88	2.37E-01	82	2.89E-01	2.8907E-01		0.02	

Table 3(b): Continued.

# θ_TOA	A&K SS	A&K SS/MS %	A&K MS	MC	VL	|A&K vs MC| %	|VL vs MC| %
#			θo_TOA = 84.26	φ_TOA = 180			
0	1.93E-02	67	2.88E-02	2.8866E-02	2.9016E-02	0.21	0.52
10	2.07E-02	67	3.09E-02	3.0413E-02	3.0566E-02	1.59	0.50
20	2.38E-02	70	3.40E-02	3.4066E-02	3.4243E-02	0.19	0.52
30	2.87E-02	73	3.93E-02	4.0087E-02	4.0276E-02	1.92	0.47
40	3.59E-02	74	4.85E-02	4.8934E-02	4.9177E-02	0.86	0.50
50	4.61E-02	75	6.15E-02	6.1830E-02	6.2124E-02	0.59	0.48
60	6.15E-02	76	8.09E-02	8.1259E-02	8.1587E-02	0.42	0.40
70	8.72E-02	78	1.12E-01	1.1378E-01	1.1407E-01	1.74	0.26
80	1.41E-01	77	1.83E-01	1.8016E-01		1.64	
85	2.00E-01	85	2.35E-01	2.4165E-01		2.63	
88	2.31E-01	88	2.63E-01	2.6380E-01		0.49	
#							
MAX %						4.69	0.52
AVER %						1.19	0.31

Table 4(a): Same as Table 3(a), except for OT=1.0.

# θ_TOA	A&K	MC	VL	|A&K vs MC| %	|VL vs MC| %
#		θo_TOA = 0	φ_TOA		
0	1.62E-01	1.6211E-01	1.6213E-01	0.07	0.01
10	1.61E-01	1.6130E-01	1.6131E-01	0.18	0.01
20	1.59E-01	1.5900E-01	1.5900E-01	0.00	0.00
30	1.56E-01	1.5562E-01	1.5564E-01	0.24	0.01
40	1.52E-01	1.5204E-01	1.5203E-01	0.03	0.01
50	1.49E-01	1.4939E-01	1.4938E-01	0.26	0.00
60	1.50E-01	1.4951E-01	1.4951E-01	0.33	0.00
70	1.55E-01	1.5464E-01	1.5464E-01	0.24	0.00
80	1.67E-01	1.6643E-01		0.34	
85	1.76E-01	1.7613E-01		0.07	
88	1.82E-01	1.8197E-01		0.02	
#		θo_TOA = 70.47	φ_TOA = 0		
0	5.22E-02	5.2141E-02	5.2148E-02	0.11	0.01
10	4.90E-02	4.8866E-02	4.8866E-02	0.28	0.00
20	4.95E-02	4.9411E-02	4.9404E-02	0.18	0.01
30	5.45E-02	5.4367E-02	5.4369E-02	0.25	0.00
40	6.49E-02	6.4761E-02	6.4758E-02	0.21	0.01
50	8.24E-02	8.2199E-02	8.2181E-02	0.25	0.02
60	1.10E-01	1.0969E-01	1.0970E-01	0.29	0.01
70	1.53E-01	1.5321E-01	1.5322E-01	0.14	0.00
80	2.27E-01	2.2629E-01		0.31	
85	2.84E-01	2.8409E-01		0.03	
88	3.27E-01	3.2691E-01		0.03	

Table 4(a): Continued.

# θ_TOA	A&K	MC	VL	|A&K vs MC| %	|VL vs MC| %
#		θo_TOA = 84.26	φ_TOA = 0		
0	1.94E-02	1.9304E-02	1.9302E-02	0.50	0.01
10	1.97E-02	1.9559E-02	1.9569E-02	0.72	0.05
20	2.17E-02	2.1609E-02	2.1620E-02	0.42	0.05
30	2.59E-02	2.5726E-02	2.5718E-02	0.68	0.03
40	3.26E-02	3.2440E-02	3.2433E-02	0.49	0.02
50	4.30E-02	4.2827E-02	4.2802E-02	0.41	0.06
60	5.96E-02	5.9317E-02	5.9353E-02	0.48	0.06
70	8.85E-02	8.8201E-02	8.8227E-02	0.34	0.03
80	1.52E-01	1.5203E-01		0.02	
85	2.27E-01	2.2708E-01		0.01	
88	3.12E-01	3.1239E-01		0.00	
#		θo_TOA = 70.47	φ_TOA = 180		
0	5.21E-02	5.2142E-02	5.2149E-02	0.08	0.01
10	5.89E-02	5.8868E-02	5.8862E-02	0.05	0.01
20	6.88E-02	6.8801E-02	6.8809E-02	0.00	0.01
30	8.20E-02	8.1990E-02	8.1999E-02	0.01	0.01
40	9.87E-02	9.8735E-02	9.8722E-02	0.04	0.01
50	1.20E-01	1.1984E-01	1.1983E-01	0.14	0.00
60	1.47E-01	1.4717E-01	1.4717E-01	0.12	0.00
70	1.85E-01	1.8501E-01	1.8502E-01	0.01	0.00
80	2.45E-01	2.4468E-01		0.13	
85	2.94E-01	2.9359E-01		0.14	
88	3.32E-01	3.3231E-01		0.09	

Table 4(a): Continued.

# θ_TOA	A&K	MC	VL	|A&K vs MC| %	|VL vs MC| %
#		θo_TOA = 84.26	φ_TOA = 180		
0	1.93E-02	1.9299E-02	1.9302E-02	0.00	0.01
10	2.07E-02	2.0702E-02	2.0704E-02	0.01	0.01
20	2.38E-02	2.3789E-02	2.3785E-02	0.05	0.02
30	2.87E-02	2.8704E-02	2.8708E-02	0.01	0.01
40	3.58E-02	3.5825E-02	3.5821E-02	0.07	0.01
50	4.60E-02	4.5964E-02	4.5996E-02	0.08	0.07
60	6.10E-02	6.1032E-02	6.0999E-02	0.05	0.05
70	8.58E-02	8.5844E-02	8.5833E-02	0.05	0.01
80	1.38E-01	1.3812E-01		0.08	
85	2.00E-01	2.0053E-01		0.26	
88	2.92E-01	2.9182E-01		0.06	
MAX %				0.72	0.07
AVER %				0.17	0.02

Table 4(b): Same as Table 3(b), except for OT=1.0

# θ_TOA	A&K SS	A&K SS/MS %	A&K MS	MC	VL	|A&K vs MC| %	|VL vs MC| %
#			θo_TOA = 0	φ_TOA			
0	1.62E-01	53	3.06E-01	3.0752E-01	3.0754E-01	0.60	0.01
10	1.61E-01	54	2.98E-01	3.0836E-01	3.0839E-01	3.31	0.01
20	1.59E-01	51	3.12E-01	3.1111E-01	3.1120E-01	0.21	0.03
30	1.56E-01	49	3.18E-01	3.1659E-01	3.1663E-01	0.56	0.01
40	1.52E-01	47	3.23E-01	3.2585E-01	3.2592E-01	0.75	0.02
50	1.49E-01	43	3.47E-01	3.4055E-01	3.4070E-01	1.75	0.05
60	1.50E-01	40	3.75E-01	3.6243E-01	3.6273E-01	3.47	0.08
70	1.55E-01	39	3.97E-01	3.8991E-01	3.9110E-01	1.93	0.31
80	1.67E-01	42	3.98E-01	4.0614E-01		2.10	
85	1.76E-01	44	4.00E-01	3.9747E-01		0.64	
88	1.82E-01	49	3.71E-01	3.7759E-01		1.63	
#			θo_TOA = 70.47	φ_TOA = 0			
0	5.22E-02	38	1.37E-01	1.3215E-01	1.3212E-01	3.95	0.03
10	4.90E-02	37	1.32E-01	1.2997E-01	1.2993E-01	1.89	0.04
20	4.95E-02	38	1.30E-01	1.3393E-01	1.3388E-01	2.74	0.04
30	5.45E-02	38	1.43E-01	1.4493E-01	1.4482E-01	1.04	0.07
40	6.49E-02	39	1.66E-01	1.6422E-01	1.6417E-01	1.33	0.03
50	8.24E-02	42	1.96E-01	1.9412E-01	1.9407E-01	1.06	0.03
60	1.10E-01	47	2.34E-01	2.3816E-01	2.3830E-01	1.73	0.06
70	1.53E-01	51	3.00E-01	3.0167E-01	3.0250E-01	0.55	0.28
80	2.27E-01	57	3.98E-01	3.8969E-01		2.20	
85	2.84E-01	65	4.37E-01	4.4304E-01		1.38	
88	3.27E-01	71	4.61E-01	4.6949E-01		1.90	

Table 4(b): Continued.

# θ_TOA	A&K SS	A&K SS/MS %	A&K MS	MC	VL	|A&K vs MC| %	|VL vs MC| %
#			$\theta o\_TOA = 84.26$	$\varphi\_TOA = 0$			
0	1.94E-02	41	4.73E-02	4.6182E-02	4.6084E-02	2.46	0.21
10	1.97E-02	42	4.69E-02	4.7059E-02	4.6982E-02	0.33	0.16
20	2.17E-02	44	4.93E-02	5.0595E-02	5.0525E-02	2.52	0.14
30	2.59E-02	48	5.40E-02	5.7169E-02	5.7091E-02	5.62	0.14
40	3.26E-02	49	6.65E-02	6.7576E-02	6.7527E-02	1.55	0.07
50	4.30E-02	51	8.43E-02	8.3321E-02	8.3204E-02	1.19	0.14
60	5.96E-02	56	1.06E-01	1.0736E-01	1.0746E-01	0.87	0.09
70	8.85E-02	60	1.48E-01	1.4695E-01	1.4749E-01	0.38	0.37
80	1.52E-01	68	2.24E-01	2.2435E-01		0.37	
85	2.27E-01	75	3.03E-01	3.0495E-01		0.70	
88	3.12E-01	82	3.81E-01	3.8657E-01		1.45	
#			$\theta o\_TOA = 70.47$	$\varphi\_TOA = 180$			
0	5.21E-02	40	1.30E-01	1.3217E-01	1.3212E-01	1.45	0.04
10	5.89E-02	43	1.37E-01	1.4004E-01	1.3997E-01	2.19	0.05
20	6.88E-02	45	1.53E-01	1.5335E-01	1.5329E-01	0.30	0.03
30	8.20E-02	48	1.71E-01	1.7226E-01	1.7226E-01	0.83	0.00
40	9.87E-02	50	1.97E-01	1.9741E-01	1.9740E-01	0.01	0.01
50	1.20E-01	52	2.31E-01	2.2996E-01	2.2997E-01	0.35	0.01
60	1.47E-01	53	2.77E-01	2.7201E-01	2.7204E-01	1.97	0.01
70	1.85E-01	56	3.30E-01	3.2695E-01	3.2715E-01	1.04	0.06
80	2.45E-01	62	3.95E-01	3.9881E-01		0.91	
85	2.94E-01	66	4.45E-01	4.4428E-01		0.26	
88	3.32E-01	71	4.68E-01	4.6891E-01		0.28	

Table 4(b): Continued.

# θ_TOA	A&K SS	A&K SS/MS %	A&K MS	MC	VL	|A&K vs MC| %	|VL vs MC| %
#			$\theta o\_TOA = 84.26$	$\varphi\_TOA = 180$			
0	1.93E-02	43	4.49E-02	4.6179E-02	4.6085E-02	2.80	0.20
10	2.07E-02	44	4.70E-02	4.7774E-02	4.7656E-02	1.53	0.25
20	2.38E-02	46	5.17E-02	5.1865E-02	5.1701E-02	0.24	0.32
30	2.87E-02	49	5.86E-02	5.8587E-02	5.8442E-02	0.03	0.25
40	3.58E-02	53	6.75E-02	6.8463E-02	6.8293E-02	1.34	0.25
50	4.60E-02	55	8.36E-02	8.2494E-02	8.2354E-02	1.38	0.17
60	6.10E-02	59	1.03E-01	1.0276E-01	1.0251E-01	0.61	0.25
70	8.58E-02	63	1.36E-01	1.3436E-01	1.3397E-01	1.36	0.29
80	1.38E-01	71	1.94E-01	1.9475E-01		0.20	
85	2.00E-01	77	2.60E-01	2.6124E-01		0.58	
88	2.92E-01	83	3.52E-01	3.5258E-01		0.22	
#							
MAX %						5.62	0.37
AVER %						1.35	0.11

Table 5(a): New results for SS away from the principal plane, OT=0.25. Columns (left to right) show: TOA VZA, followed by MYSTIC (MC), VLIDORT (VL), and relative deviations of the two. The sequence of TOA relative azimuths (top to bottom) is φ = 45°, 90°, 135°.

# θ_TOA	MC	VL	|VL vs MC| %
#	θo_TOA = 70.47	φ_TOA = 45	
0	3.3338E-02	3.3331E-02	0.02
10	3.1814E-02	3.1813E-02	0.00
20	3.2010E-02	3.2011E-02	0.00
30	3.4297E-02	3.4297E-02	0.00
40	3.9359E-02	3.9365E-02	0.02
50	4.8555E-02	4.8547E-02	0.02
60	6.4791E-02	6.4804E-02	0.02
70	9.5982E-02	9.5984E-02	0.00
80	1.9370E-01		
85	2.2488E-01		
88	1.7797E-01		
#	θo_TOA = 84.26	φ_TOA = 45	
0	1.9262E-02	1.9261E-02	0.01
10	1.9432E-02	1.9427E-02	0.02
20	2.0795E-02	2.0798E-02	0.01
30	2.3598E-02	2.3600E-02	0.01
40	2.8277E-02	2.8291E-02	0.05
50	3.5815E-02	3.5820E-02	0.01
60	4.8371E-02	4.8396E-02	0.05
70	7.2312E-02	7.2307E-02	0.01
80	1.5171E-01		
85	2.0564E-01		
88	1.7939E-01		
#	θo_TOA = 70.47	φ_TOA = 90	
0	3.3332E-02	3.3331E-02	0.00
10	3.3695E-02	3.3695E-02	0.00
20	3.4854E-02	3.4846E-02	0.02
30	3.7000E-02	3.6989E-02	0.03
40	4.0571E-02	4.0563E-02	0.02
50	4.6440E-02	4.6433E-02	0.01
60	5.6542E-02	5.6544E-02	0.00
70	7.6066E-02	7.6066E-02	0.00
80	1.3795E-01		
85	1.5866E-01		
88	1.2451E-01		

Table 5(a): Continued.

# θ_TOA	MC	VL	|VL vs MC| %
#	**θ_TOA = 84.26**	**φ_TOA = 90**	
0	1.9264E-02	1.9261E-02	0.01
10	1.9528E-02	1.9530E-02	0.01
20	2.0368E-02	2.0374E-02	0.03
30	2.1924E-02	2.1927E-02	0.01
40	2.4470E-02	2.4476E-02	0.03
50	2.8604E-02	2.8600E-02	0.01
60	3.5621E-02	3.5628E-02	0.02
70	4.9174E-02	4.9162E-02	0.02
80	9.0296E-02		
85	1.2919E-01		
88	1.1919E-01		
#	**θo_TOA = 70.47**	**φ_TOA = 135**	
0	3.3340E-02	3.3331E-02	0.03
10	3.6389E-02	3.6386E-02	0.01
20	4.0953E-02	4.0959E-02	0.01
30	4.7221E-02	4.7218E-02	0.01
40	5.5640E-02	5.5650E-02	0.02
50	6.7307E-02	6.7314E-02	0.01
60	8.4707E-02	8.4725E-02	0.02
70	1.1465E-01	1.1462E-01	0.03
80	1.9707E-01		
85	2.3109E-01		
88	1.8140E-01		
#	**θ_TOA = 84.26**	**φ_TOA = 135**	
0	1.9268E-02	1.9261E-02	0.03
10	2.0205E-02	2.0206E-02	0.00
20	2.2271E-02	2.2274E-02	0.01
30	2.5606E-02	2.5603E-02	0.01
40	3.0547E-02	3.0539E-02	0.03
50	3.7810E-02	3.7798E-02	0.03
60	4.9031E-02	4.9035E-02	0.01
70	6.8546E-02	6.8549E-02	0.00
80	1.1351E-01		
85	1.6542E-01		
88	1.7560E-01		
#			
MAX %			**0.05**
AVER %			**0.02**

Table 5(b): Same as Table 5(a), except for MS.

# θ_TOA	MC	VL	|VL vs MC| %
#	θo_TOA = 70.47	φ_TOA = 45	
0	4.8720E-02	4.8822E-02	0.21
10	4.7458E-02	4.7587E-02	0.27
20	4.8618E-02	4.8741E-02	0.25
30	5.2649E-02	5.2776E-02	0.24
40	6.0484E-02	6.0644E-02	0.26
50	7.3983E-02	7.4194E-02	0.28
60	9.7304E-02	9.7571E-02	0.27
70	1.4129E-01	1.4184E-01	0.39
80	2.7906E-01		
85	3.0631E-01		
88	2.2969E-01		
#	θo_TOA = 84.26	φ_TOA = 45	
0	2.8871E-02	2.9016E-02	0.50
10	2.9270E-02	2.9415E-02	0.49
20	3.1302E-02	3.1454E-02	0.48
30	3.5272E-02	3.5447E-02	0.49
40	4.1790E-02	4.2027E-02	0.56
50	5.2253E-02	5.2511E-02	0.49
60	6.9587E-02	6.9956E-02	0.53
70	1.0250E-01	1.0308E-01	0.57
80	2.1262E-01		
85	2.6667E-01		
88	2.1752E-01		
#	θo_TOA = 70.47	φ_TOA = 90	
0	4.8725E-02	4.8823E-02	0.20
10	4.9369E-02	4.9486E-02	0.24
20	5.1457E-02	5.1570E-02	0.22
30	5.5235E-02	5.5392E-02	0.28
40	6.1462E-02	6.1636E-02	0.28
50	7.1460E-02	7.1661E-02	0.28
60	8.8268E-02	8.8524E-02	0.29
70	1.1988E-01	1.2042E-01	0.45
80	2.1880E-01		
85	2.3630E-01		
88	1.7418E-01		

Table 5(b): Continued.

# θ_TOA	MC	VL	|VL vs MC|
#	θ_TOA = 84.26	φ_TOA = 90	
0	2.8867E-02	2.9016E-02	0.51
10	2.9323E-02	2.9474E-02	0.51
20	3.0763E-02	3.0910E-02	0.47
30	3.3346E-02	3.3529E-02	0.55
40	3.7572E-02	3.7774E-02	0.53
50	4.4283E-02	4.4541E-02	0.58
60	5.5520E-02	5.5880E-02	0.64
70	7.6798E-02	7.7330E-02	0.69
80	1.4128E-01		
85	1.8190E-01		
88	1.5386E-01		
#	θo_TOA = 70.47	φ_TOA = 135	
0	4.8701E-02	4.8823E-02	0.25
10	5.2132E-02	5.2229E-02	0.19
20	5.7678E-02	5.7816E-02	0.24
30	6.5726E-02	6.5865E-02	0.21
40	7.6942E-02	7.7106E-02	0.21
50	9.2890E-02	9.3090E-02	0.22
60	1.1713E-01	1.1744E-01	0.27
70	1.5936E-01	1.5984E-01	0.30
80	2.7701E-01		
85	3.0915E-01		
88	2.3206E-01		
#	θo_TOA = 84.26	φ_TOA = 135	
0	2.8869E-02	2.9016E-02	0.50
10	2.9955E-02	3.0131E-02	0.58
20	3.2613E-02	3.2785E-02	0.52
30	3.6990E-02	3.7177E-02	0.50
40	4.3575E-02	4.3797E-02	0.51
50	5.3395E-02	5.3639E-02	0.45
60	6.8633E-02	6.8969E-02	0.49
70	9.5135E-02	9.5542E-02	0.43
80	1.5549E-01		
85	2.1035E-01		
88	2.0870E-01		
#			
MAX %			0.69
AVER %			0.39

Table 6(a): Same as Table 5(a), except for OT=1.0.

# θ_TOA	MC	VL	|VL vs MC| %
#	θo_TOA = 70.47	φ_TOA = 45	
0	5.2144E-02	5.2148E-02	0.01
10	4.9700E-02	4.9693E-02	0.01
20	4.9697E-02	4.9699E-02	0.01
30	5.2638E-02	5.2635E-02	0.01
40	5.9255E-02	5.9260E-02	0.01
50	7.0845E-02	7.0835E-02	0.01
60	8.9741E-02	8.9747E-02	0.01
70	1.2059E-01	1.2059E-01	0.00
80	1.7400E-01		
85	2.1737E-01		
88	2.5008E-01		
#	θo_TOA = 84.26	φ_TOA = 45	
0	1.9299E-02	1.9302E-02	0.01
10	1.9445E-02	1.9438E-02	0.04
20	2.0759E-02	2.0756E-02	0.02
30	2.3440E-02	2.3461E-02	0.09
40	2.7940E-02	2.7947E-02	0.03
50	3.5009E-02	3.5023E-02	0.04
60	4.6449E-02	4.6470E-02	0.05
70	6.6867E-02	6.6852E-02	0.02
80	1.1277E-01		
85	1.6791E-01		
88	2.3311E-01		
#	θo_TOA = 70.47	φ_TOA = 90	
0	5.2143E-02	5.2148E-02	0.01
10	5.2606E-02	5.2605E-02	0.00
20	5.4040E-02	5.4041E-02	0.00
30	5.6674E-02	5.6669E-02	0.01
40	6.0920E-02	6.0926E-02	0.01
50	6.7579E-02	6.7586E-02	0.01
60	7.8124E-02	7.8125E-02	0.00
70	9.5537E-02	9.5544E-02	0.01
80	1.2692E-01		
85	1.5378E-01		
88	1.7472E-01		

Table 6(a): Continued.

# θ_TOA	MC	VL	|VL vs MC| %
#	θ_TOA = 84.26	φ_TOA = 90	
0	1.9298E-02	1.9302E-02	0.02
10	1.9563E-02	1.9561E-02	0.01
20	2.0376E-02	2.0374E-02	0.01
30	2.1868E-02	2.1863E-02	0.02
40	2.4278E-02	2.4286E-02	0.03
50	2.8156E-02	2.8155E-02	0.00
60	3.4591E-02	3.4598E-02	0.02
70	4.6448E-02	4.6422E-02	0.06
80	7.3936E-02		
85	1.0824E-01		
88	1.5321E-01		
#	θo_TOA = 70.47	φ_TOA = 135	
0	5.2145E-02	5.2148E-02	0.01
10	5.6768E-02	5.6777E-02	0.02
20	6.3459E-02	6.3451E-02	0.01
30	7.2223E-02	7.2216E-02	0.01
40	8.3399E-02	8.3404E-02	0.01
50	9.7734E-02	9.7737E-02	0.00
60	1.1681E-01	1.1683E-01	0.01
70	1.4406E-01	1.4405E-01	0.00
80	1.8845E-01		
85	2.2532E-01		
88	2.5428E-01		
#	θ_TOA = 84.26	φ_TOA = 135	
0	1.9302E-02	1.9302E-02	0.00
10	2.0247E-02	2.0260E-02	0.06
20	2.2316E-02	2.2322E-02	0.03
30	2.5619E-02	2.5613E-02	0.02
40	3.0470E-02	3.0460E-02	0.03
50	3.7539E-02	3.7519E-02	0.05
60	4.8275E-02	4.8293E-02	0.04
70	6.6561E-02	6.6553E-02	0.01
80	1.0617E-01		
85	1.5427E-01		
88	2.2294E-01		
#			
MAX %			0.09
AVER %			0.02

Table 6(b): Same as Table 5(b), except for OT=1.0.

# θ_TOA	MC	VL	|VL vs MC| %
#	θo_TOA = 70.47	φ_TOA = 45	
0	1.3213E-01	1.3212E-01	0.01
10	1.3077E-01	1.3071E-01	0.05
20	1.3408E-01	1.3399E-01	0.06
30	1.4270E-01	1.4267E-01	0.02
40	1.5786E-01	1.5787E-01	0.00
50	1.8141E-01	1.8134E-01	0.04
60	2.1605E-01	2.1614E-01	0.04
70	2.6581E-01	2.6657E-01	0.28
80	3.3318E-01		
85	3.7201E-01		
88	3.8894E-01		
#	θo_TOA = 84.26	φ_TOA = 45	
0	4.6195E-02	4.6084E-02	0.24
10	4.6864E-02	4.6752E-02	0.24
20	4.9525E-02	4.9430E-02	0.19
30	5.4521E-02	5.4443E-02	0.14
40	6.2441E-02	6.2374E-02	0.11
50	7.4442E-02	7.4386E-02	0.08
60	9.2827E-02	9.2855E-02	0.03
70	1.2300E-01	1.2334E-01	0.27
80	1.8117E-01		
85	2.4139E-01		
88	3.0347E-01		
#	θo_TOA = 70.47	φ_TOA = 90	
0	1.3213E-01	1.3212E-01	0.01
10	1.3365E-01	1.3360E-01	0.04
20	1.3821E-01	1.3817E-01	0.03
30	1.4627E-01	1.4624E-01	0.03
40	1.5858E-01	1.5857E-01	0.01
50	1.7638E-01	1.7639E-01	0.01
60	2.0152E-01	2.0164E-01	0.06
70	2.3631E-01	2.3689E-01	0.25
80	2.8002E-01		
85	3.0258E-01		
88	3.0867E-01		

Table 6(b): Continued.

# θ_TOA	MC	VL	|VL vs MC| %
#	θ_TOA = 84.26	φ_TOA = 90	
0	4.6193E-02	4.6084E-02	0.24
10	4.6799E-02	4.6709E-02	0.19
20	4.8750E-02	4.8643E-02	0.22
30	5.2198E-02	5.2095E-02	0.20
40	5.7598E-02	5.7486E-02	0.19
50	6.5700E-02	6.5592E-02	0.16
60	7.8053E-02	7.7971E-02	0.11
70	9.7934E-02	9.7932E-02	0.00
80	1.3531E-01		
85	1.7406E-01		
88	2.1719E-01		
#	θo_TOA = 70.47	φ_TOA = 135	
0	1.3214E-01	1.3212E-01	0.02
10	1.3788E-01	1.3784E-01	0.03
20	1.4778E-01	1.4777E-01	0.00
30	1.6215E-01	1.6211E-01	0.03
40	1.8154E-01	1.8148E-01	0.03
50	2.0703E-01	2.0701E-01	0.01
60	2.4061E-01	2.4069E-01	0.03
70	2.8480E-01	2.8507E-01	0.10
80	3.4116E-01		
85	3.7422E-01		
88	3.8895E-01		
#	θ_TOA = 84.26	φ_TOA = 135	
0	4.6197E-02	4.6085E-02	0.24
10	4.7364E-02	4.7276E-02	0.18
20	5.0424E-02	5.0328E-02	0.19
30	5.5579E-02	5.5418E-02	0.29
40	6.3197E-02	6.3017E-02	0.28
50	7.4178E-02	7.3973E-02	0.28
60	9.0271E-02	9.0085E-02	0.21
70	1.1555E-01	1.1528E-01	0.24
80	1.6362E-01		
85	2.1586E-01		
88	2.8408E-01		
#			
MAX %			0.29
AVER %			0.12

Table 7: See in the text, page 11.